Coupled THCM model of a heating and hydration concrete-bentonite column test

J. Samper [1)], A. Mon[1)], L. Montenegro [1)], J. Cuevas[2)], M.J. Turrero[3)], A. Naves [1)], R. Fernández[2)], E. Torres[3)]

[1)] Centro de Investigaciones Científicas Avanzadas (CICA), E.T.S. Ingenieros de Caminos, Canales y Puertos, Campus de Elviña, University of A Coruña, 15071 La Coruña, Spain
[2)] Facultad de Ciencias. Universidad Autónoma de Madrid, Spain
[3)] Centro de Investigaciones Energéticas, Medio Ambientales y Tecnológicas, 28040, Madrid, Spain

Corresponding author: J. Samper, email: j.samper@udc.es

Abstract

Radioactive waste disposal in deep geological repositories in clay formations envisage a compacted bentonite engineered barrier and a concrete liner. The alkaline conditions caused by the degradation of concrete could affect the performance of the engineered barrier. The geochemical interactions occurring at the concrete-bentonite interface (B-CI) for the non-isothermal unsaturated conditions prevailing at repository post-closure have been studied by CIEMAT with a heating and hydration concrete-bentonite column test. The column consists of a 3 cm thick concrete sample emplaced on top of a 7.15 cm block of compacted bentonite. The column was hydrated through the concrete at a constant pressure with a synthetic clay porewater while the bottom of the column was heated at 100ºC. Here we report a coupled thermo-hydro-chemical-mechanical (THCM) model of the column test, which lasted 1610 days. The model was solved with a THCM code, INVERSE-FADES-CORE. Experimental observations show calcite and brucite precipitation in the concrete near the hydration boundary, portlandite dissolution and calcite and ettringite precipitation in the concrete, calcite and sepiolite precipitation in the

bentonite near the B-CI, calcite dissolution in the bentonite far from the B-CI and gypsum precipitation in the bentonite near the heater. Model results attest that advection is relevant during the first months of the test. Later, solute diffusion becomes the dominant transport mechanism. Calcite and brucite precipitate in the concrete near the hydration boundary because the concentrations of dissolved bicarbonate and magnesium in the hydration water are larger than the initial concentrations in the concrete porewater. Calcite and brucite precipitate in both sides of the B-CI. Sepiolite precipitates in the bentonite near the B-CI. The model predicts portlandite and C1.8SH dissolution in the concrete. Ettringite and C0.8SH precipitate near the hydration boundary while ettringite dissolves in the rest of the concrete at very small rates. The porosity changes at the hydration boundary and at both sides of the B-CI due to mineral dissolution/precipitation occur. The porosity reduces to zero in a 0.03 cm thick zone in the concrete near the B-CI due to brucite and calcite precipitation. The high pH front (pH > 8.5) diffuses from the concrete into the bentonite and penetrates 1 cm at the end of the test after 1610 days. Model results are sensitive to grid size. Mineral precipitation and the thickness of the zone affected by mineral precipitation in the bentonite near the B-CI increase when the grid size increases while pore clogging in the concrete near the B-CI is computed only for grid sizes smaller than 0.018 cm. The non-isothermal conditions play an important role in mineral precipitation. The reduction in porosity in the B-CI for constant temperature is smaller than that of the non-isothermal run. The model reproduces the on-line measured temperature and relative humidity data as well as the water content and porosity data collected at the end of the test. Model results capture the main trends of the mineralogical observations, except for ettringite and CSH phases for which the predicted precipitation is smaller than the observed values. Model results improve when the specific surface of ettringite is increased by a factor of 10.

Key words: THCM model, concrete, FEBEX bentonite, alkaline front, reactive transport, porosity clogging

1 Introduction

Compacted bentonite is a backfill and sealing material for high-level radioactive waste (HLW) disposal in deep geological repositories. A concrete liner will be the support of the galleries in the Spanish reference concept for disposal in a clay host rock (ENRESA, 2004). Concrete is a source of alkaline solutions, which may reduce drastically the porosity at the interfaces of concrete with other materials due to the precipitation of mineral phases.

The interactions of concrete and clay barriers have been studied in laboratory and in situ experiments (Melkior *et al*., 2004; Gaucher and Blanc, 2006; Yamaguchi *et al*., 2007; Fernández *et al*., 2009b; Savage *et al*., 2011; Lalan at al., 2016; Cuevas at al., 2016; Dauzères *et al*., 2016; Watson *et al*., 2016; Alonso *et al*., 2017; Balmer at al., 2017; Fernández at al., 2017; Lothenbach *et al*., 2017) and industrial and natural analogues (Steefel and Lichtner, 1998; Gaucher and Blanc, 2006; Savage *et al*., 2010; Savage, 2011; Soler, 2013; Watson *et al*., 2013; Watson *et al*., 2016).

Extensive reactive transport modelling studies of the long-term cement-bentonite interactions and the effects of the alkaline plume have been performed during the last 25 years (De Windt *et al*., 2004; Yamaguchi *et al*., 2007; Yang *et al*., 2008a; Fernández *et al*., 2009a; Marty *et al*., 2009; Watson *et al*., 2009; Berner *et al*., 2013; Kosakowski and Berner, 2013; Shao *et al*., 2013; Watson *et al*., 2013; Marty *et al*., 2015, De Windt *et al* 2016; Mon *et al*., 2017).

Coupled thermal, hydrodynamic, chemical and mechanical models are needed to simulate the complex interplays among THCM phenomena during the initial stages of a geological repository when non-isothermal unsaturated flow in deformable media take place simultaneously with chemical reactions (Samper *et al*., 2008a; Zheng and Samper, 2008; Zheng *et al*., 2008a; 2008b; 2010; 2011).

CIEMAT performed a set of column tests to study the interactions of concrete and compacted bentonite at the conditions prevailing in the engineered barrier system of a geological repository during the early hydration stage (Turrero *et al*., 2011; Torres *et al*., 2013). The columns containing the concrete and bentonite samples were hydrated at a constant pressure at the top of the column through the concrete while the temperature was maintained constant at 100ºC at the bottom of the column. Here we present a coupled thermo-hydro-chemical-mechanical (THCM) model of the heating and hydration concrete-bentonite column test on the HB4 column test. The paper starts with the description of the HB4 column test. Then, the conceptual and numerical model and the computer code are presented. Next, the main results of the THCM numerical model are discussed. The results of the sensitivity runs are also presented. Afterwards, a comparison of the model results to experimental mineralogical data is presented.

2 Test description and available data

Six heating and hydration experiments on concrete-bentonite columns (HB column tests) were performed on May 2006 at the CIEMAT facilities in Madrid (Spain) to study the interactions of concrete and bentonite (Turrero *et al*., 2011; Torres *et al*., 2013). These column tests were dismantled sequentially after 6 (HB1), 12 (HB2), 18 (HB3), 54 (HB4), 80 (HB5) and 121 (HB6) months.

The tests were carried out on medium-size cells containing a cylinder of bentonite, with a height of 7.15 cm and a radius of 3.5 cm, in contact with a cylinder of concrete, with a height of 3 cm and a radius of 3.5 cm. The bentonite and the concrete samples were emplaced into cylindrical hermetic cells with an internal diameter of 7 cm and an inner length of 10 cm (Figure 1). The outer cells were made of Teflon to decrease the lateral heat conduction and framed with clamps to prevent bentonite swelling. A temperature of 100ºC was imposed at the bottom of the column through a plane stainless steel heater while on the top of the column a hydration system allowed the circulation of water through a stainless steel tank at a controlled temperature. The tank was periodically weighed to check the water intake. There was no gas or liquid flux at the bottom of the column.

The FEBEX bentonite was compacted with a gravimetric water content of 14% at a dry density of 1.65 g/cm^3. The concrete sample was prepared with a sulforesistant ordinary Portland cement (CEM I-SR). The cement paste was Cement I-42.5 R/SR.T. The receipt was done with 400 kg of cement, 911 kg of sand (0-5 mm), and 946 kg of aggregates (6-16 mm) with a w/c ratio of 0.45. The dry density of the concrete was 2.22 g/cm^3 and the initial gravimetric water content was equal to 2.6%. The concrete-bentonite column tests were hydrated with synthetic Spanish Reference Clay porewater (Turrero *et al.*, 2011).

The column tests were instrumented with two capacitive sensors to record the relative humidity and the temperature in the bentonite at 5 cm (sensor 1) and 9.5 cm (sensor 2) from the hydration system (Figure 1). The relative humidity data recorded in the sensor located near the heater (sensor 2) might not be reliable because the data could be affected by vapour leakage through the sensor openings (Turrero *et al.*, 2011).

The HB4 column test was dismantled at ambient temperature after 1610 days of heating and hydration. Special attention was given to preserve and characterize properly

the concrete-bentonite interface (B-CI). Then, the 3 cm-thick sample of concrete and a 1.5 cm-thick bentonite slice were wrapped together and isolated with a parafilm layer. The remaining part of the compacted bentonite cylinder was cut into four sections. A detailed description of the sampling and post-mortem analyses can be found in Turrero *et al*. (2011).

The final distribution of the water content, the dry density and the porosity were measured at the end of the test at several locations in the bentonite. The concentrations of dissolved species and exchanged cations were measured also at the end of the HB4 column test. The aqueous extract test (AET) method was used to obtain the porewater chemistry of the compacted bentonite. Bentonite samples were placed in contact with deionised and degassed water at a solid to liquid ratio of 1:8 (5 mg of clay in 40 mL of water) and stirred during 24 hours. Chemical analyses were performed on supernatant solution after phase separation by centrifugation (Turrero *et al*., 2011). Besides dilution, several chemical reactions take place during porewater extraction from clay samples, which change the concentrations of dissolved species in a complex nonlinear manner. This makes it difficult to derive the chemical composition of the original (before aqueous extraction) clay porewater from aqueous extract data (Bradbury and Baeyens, 1998; Sacchi *et al*. 2001).

The mineral phases in the concrete and in the bentonite samples at the end of the HB4 column test were characterized by FTIR, XRD and SEM techniques (Turrero *et al*., 2011). The main experimental observations are listed in Table 1.

3 THCM model

3.1 Conceptual model

The mathematical formulation of the flow and transport model of the HB4 column test is similar to that used by Zheng *et al*. (2010; 2011) for the heating and hydration experiments performed in FEBEX bentonite samples. The multiphase flow model accounts for: 1) Coupled flow of liquid water due to hydraulic, chemical and thermal gradients, 2) Vapor advection and diffusion, 3) Advection and diffusion of 'dry' air, 4) Flow of air dissolved in the water (advection), and 5) Heat convection through the liquid and gaseous phases and heat conduction through the solid, liquid and gaseous phases. The model assumes that there is equilibrium between: 1) The liquid and the vapor phase according to the Kelvin equation, 2) The temperature of the phases with instantaneous dissipation of thermal perturbations; 3) Air in the liquid and gaseous phases, and 4) Vapor and 'dry' air. The air partial pressure is related to the mass fraction of the air in the liquid phase through Henry's law.

Water flow, heat transfer and solute transport occur mostly in one-dimension parallel to the axis of the column. Therefore, the test was modelled with a 1-D mesh (Figure 2). The model domain includes the concrete (0 < x < 3 cm) and the compacted bentonite (3 cm < x < 10.15 cm).

Although the column test constrained the deformation of the bentonite, the swelling of the bentonite is allowed in the model to simulate the measured deformation. Bentonite swelling is modelled with the following state-surface expression of Lloret and Alonso (1995):

$$e = A + B ln\sigma' + C ln(\Psi + p^a) + D ln\sigma' \ln(\Psi + p^a) \quad (1)$$

where e is the void ratio which is equal to the volume of voids divided by the volume of the solids; p^a is the atmospheric pressure in Pa, σ' is the mean effective stress in Pa; Ψ is

suction in Pa, and A, B, C and D are empirical constants which for FEBEX compacted bentonite are A=0.76, B=-0.052446, C=-0.0406413 and D= 0.00479977 (Nguyen *et al.*, 2005). No concrete vertical displacement is allowed in the model.

The conceptual geochemical model includes the following reactions: 1) Aqueous complexation; 2) Acid/base; 3) Mineral dissolution/precipitation, 4) Cation exchange of Ca^{2+}, Mg^{2+}, Na^{+} and K^{+} only in the bentonite and 5) Surface complexation of H^{+} on three types of sorption sites ($S^{S}OH$, $S^{W1}OH$ and $S^{W2}OH$) only in the bentonite. The aqueous chemical system includes the following 11 primary species: H_2O, H^{+}, Ca^{2+}, Mg^{2+}, Na^{+}, K^{+}, Cl^{-}, SO_4^{2-}, HCO_3^{-}, SiO_2(aq) and Al^{3+}. The model considers 12 minerals and 39 aqueous complexes identified from speciation runs performed with EQ3/6 (Wolery, 1992) (see Table 2). The Gaines-Thomas convention was used for modelling cation exchange reactions. Surface complexation reactions were modelled with the triple sorption site model of Bradbury and Baeyens (1997; 1998; 2003). Chemical reactions and the equilibrium constants at 25ºC for aqueous species and mineral dissolution/precipitation as well as the selectivity coefficients for cation exchange and the protolysis constants for surface complexation are listed in Table 2. The equilibrium constants for aqueous complexes and minerals, K, depend on temperature, T, according to (Wolery, 1992):

$$\log K(T) = \frac{b_1}{T^2} + \frac{b_2}{T} + b_3 \ln T + b_4 + b_5 T \qquad (2)$$

where b_1 to b_5 are coefficients which are derived by fitting Eq. 2 to measured log K values at 0, 25, 60, 100, 150, 200, 250 and 300ºC. This expression is valid for $0 < T < 300$ ºC.

All the reactions except the dissolution/precipitation of portlandite, ettringite, C1.8SH, C0.8SH, quartz and cristobalite are assumed at chemical equilibrium. Kinetic mineral dissolution/precipitation is modelled with the following rate law:

$$r_m = k_m e^{-\frac{Ea}{RT}}({\Omega_m}^{\theta} - 1)^{\eta}(a_{H^+})^n \quad (3)$$

where r_m is the dissolution/precipitation rate (mol/m^2/s); k_m is the kinetic rate constant (mol/m^2/s) at 25ºC, Ω_m is the ratio between the ion activity product and the equilibrium constant (dimensionless) and θ and η are parameters of the kinetic law. The term $e^{-\frac{Ea}{RT}}$ is the thermodynamic factor, which takes into account the apparent activation energy of the reaction, *Ea*, and *R* and *T* are the gas constant and the absolute temperature, respectively. The term $(a_{H^+})^n$ is only used for quartz and includes the proton activity, a_{H^+}, raised to the power *n*.

The dissolution/precipitation rate in mol/m^2/s, r_m, is multiplied by the mineral specific surface area, σ, to get the dissolution/precipitation rate in mol/m^3/s, R_m. The specific surface area σ is defined as the surface area of the mineral per unit fluid volume. The model assumes that σ remains constant.

The model does not consider smectite dissolution because we claim that its dissolution is too slow in short time tests, although it has been demonstrated to be important when the objective is to compare the long-term laboratory and natural scenarios (Drever, 1998; White and Brantley, 2003; Hunt *et al.*, 2015).

3.2 Numerical model

The finite element mesh has 196 nodes in the concrete and 255 nodes in the bentonite (Figure 2). The mesh discretization is non-uniform, being more refined near the B-CI. The grid size, Δx, is equal to 0.05 cm near the hydration boundary (0 cm < x < 0.75 cm), 0.025 cm in the central zone of the concrete (0.75 cm < x < 1.5 cm), 0.01 cm at both sides of the B-CI (1.5 cm < x < 4.45 cm), 0.025 cm in the interval 4.45 cm < x < 5.25 cm,

0.05 cm in the interval 5.25 cm < x < 7.75 cm and 0.087 cm near the heater (7.75 cm < x <10.15 cm).

The numerical model simulates the 1610 days of heating and hydration and 2 days of cooling during which hydration was stopped and the temperature was switched to ambient temperature. The simulation of the cooling stage is required to account for the effects of the cooling on mineral dissolution/precipitation. The model takes into account also the cooling stage after the test, when the final distribution of the water content, the dry density, the porosity, the aqueous extract data and mineralogical observations in the bentonite samples were performed.

The thermal, hydrodynamic and mechanical parameters of the bentonite were taken from those reported for the numerical models of the FEBEX *mock-up test* (Zheng and Samper, 2008) and a heating and hydration test on FEBEX bentonite (Zheng *et al*., 2010). The thermo-osmosis permeability was derived from Zheng *et al*. (2010) and is equal to $4.2 \cdot 10^{-13}$ $m^2/K/s$. The porewater diffusion coefficient is equal to $2 \cdot 10^{-10}$ m^2/s for all aqueous species, except for Cl^-, which has a diffusion coefficient of $9.2 \cdot 10^{-11}$ m^2/s. The effective diffusion coefficient of all the aqueous species is equal to $9.45 \cdot 10^{-12}$ m^2/s in the bentonite and $5.3 \cdot 10^{-13}$ m^2/s in the concrete. The effective diffusion of Cl^- is equal to $4.25 \cdot 10^{-12}$ m^2/s in the bentonite and $2.4 \cdot 10^{-13}$ m^2/s in the concrete. Similar to Zheng *et al*. (2010), the THCM model does not consider anion exclusion.

Concrete parameters were taken from Ayora *et al*. (2007) and derived from laboratory experiments (Villar *et al*., 2012; Villar, 2013). Hydrodynamic, mechanical, thermal and solute parameters of the bentonite and the concrete are listed in Tables 3 to 6.

The boundary conditions of the model are shown in Figure 2. The temperatures were prescribed at the boundaries of the numerical model. The temperature in the

hydration boundary (x = 0) is assumed to be 25ºC. The prescribed temperature at the bottom of the column, where the heater is located, is 90ºC. This temperature is lower than the heater temperature due to lateral heat losses. Heat dissipation at the location of the sensors was modelled with a Cauchy condition according to which the heat outflux, Q_c, is computed from

$$Q_c = \alpha_T (T - T^*) \tag{4}$$

where α_T is the thermal coefficient which is equal to 1016 W/ºC (Mon, 2017) and T^* is the external temperature which is equal to the mean temperature measured in the temperature sensors. A Neuman transport boundary condition was used for solute transport according to which solute flux is equal to the product of water flux times solute concentration of inflow water.

The initial porosity of the bentonite is 0.4 and the initial volumetric water content is 0.228, which corresponds to a saturation degree of 57% and a suction of $1.27 \cdot 10^8$ Pa. The concrete has a porosity of 0.125, an initial volumetric water content of 0.0484 and a saturation degree of 38.7%. The initial temperature in the column is 22ºC. The gas pressure is the atmospheric pressure during the test. The initial stress is assumed uniform and isotropic and equal to $2.5 \cdot 10^5$ Pa. The liquid pressure in the injection tank was initially equal to 500 kPa. It decreased after 400 days due to problems in the water injection system. The liquid pressure at the injection boundary was assumed equal to 500 kPa for t < 400 days and 100 kPa afterwords.

The initial composition of the bentonite porewater was derived from Fernández *et al.* (2001). The Al^{3+} concentration in bentonite porewater was taken from ENRESA (2000). The initial composition of the concrete porewater was calculated with EQ3/6 (Wollery, 1992) based on the concrete porewater of ENRESA (2004) and by assuming that the concentration of dissolved Ca^{2+} is at local chemical equilibrium with respect to

portlandite, HCO_3^- is at equilibrium with respect to calcite, Mg^{2+} is equilibrated with brucite, SO_4^{2-} is equilibrated with ettringite and SiO_2(aq) is equilibrated with C1.8SH. The injection water is a synthetic Spanish Reference Clay porewater (Turrero *et al.*, 2011). It should be pointed out that the concentrations of Mg^{2+}, Ca^{2+} and HCO_3^- in the injected water are larger than those of the initial concrete porewater. The chemical composition of the injected water and the initial bentonite and concrete porewaters are listed in Table 7.

The initial mineral volume fractions in the bentonite are: 0.36% for calcite, 0.0829% for gypsum, 1.18% for cristobalite; and 57% for the noneactive smectite. The initial volume fractions of the concrete are: 0.1% for calcite, 7.4% for portlandite, 1% for brucite, 14.6% for C1.8SH1.8, 2.2% for ettringite and 62.2% for quartz. The secondary minerals allowed to precipitate include: anhydrite, sepiolite, C0.8SH and anorthite.

The activation energy, the kinetic rate constants and the mineral specific surfaces were taken from Fernández *et al.* (2009a). The specific surfaces of some minerals were calibrated to reproduce the experimental mineralogical observations. The kinetic parameters of portlandite, ettringite, C1.8SH, C0.8SH, quartz and cristobalite are listed in Table 8.

The cation exchange capacity (CEC) of the bentonite is 102 meq/100g (Fernández *et al.*, 2004). Cation selectivity coefficients for exchanged Ca^{2+}, Mg^{2+} and K^+ were derived from ENRESA (2006b). These coefficients were calibrated to reproduce the concentrations of exchanged cations reported by Fernández *et al.* (2004) for the FEBEX bentonite (Table 2). The total concentration of the sorption sites in the bentonite is 0.629 mol/L (Bradbury and Baeyens, 1997). Strong sites have a strong binding affinity but a small concentration of 0.015 mol/L. The other two types are the weak #1 and #2 sites which have binding constants weaker than those of the strong sites although their

concentrations (0.307 mol/L) are larger than those of the strong sites. Surface complexation and cation exchange reactions take place only in the bentonite.

3.3 Computer code

The model was performed with the code INVERSE-FADES-CORE V2 (Zheng *et al*., 2010; Zheng and Samper, 2015; Mon, 2017). INVERSE-FADES-CORE is a finite element code for modelling non-isothermal multiphase flow, heat transport and multicomponent reactive solute transport under both chemical equilibrium and kinetics conditions. INVERSE-FADES-CORE solves both forward and inverse multiphase flow and multicomponent reactive transport problems in 1-, 2- and 3-D axi-symmetric porous and fractured media This code is the result of integrating the capabilities of FADES (Navarro, 1997), CORE^{2D} (Samper *et al*., 2003; 2009; 2011), FADES-CORE (ENRESA, 2000) and INVERSE-CORE (Dai and Samper, 2004; Yang *et al*., 2008b; Yang *et al*., 2014). State variables of the forward model include liquid and gas pressures and temperature, which are solved by a Newton–Raphson method. A sequential iteration method is used to solve reactive transport equations.

The concentrations of secondary species are computed from the concentrations of primary species through appropriate mass action laws (Xu *et al*., 1999). The concentrations of precipitated, exchanged and adsorbed species are computed using similar equations. A detailed description of calculations of chemical reactions can be found in Xu *et al*. (1999).

The forward routines of INVERSE-FADES-CORE have been widely verified with analytical solutions and tested with THM and THC problems (Navarro and Alonso, 2000; ENRESA, 2000; Samper *et al*., 2008a) as well as with THMC phenomena (Zheng, 2006). Codes of CORE^{2D} series have been used to model FEBEX laboratory tests (Samper *et al*., 2006, 2008b; Zheng *et al*., 2010), in situ tests (Zhang *et al*., 2008; Soler *et al*., 2008; Zheng *et al*., 2011; Zheng and Samper, 2015), field case studies (Molinero *et al*., 2004;

Dai and Samper, 2004; Molinero and Samper, 2006; Dai and Samper, 2006; Dai *et al.*, 2006), evaluate the long-term geochemical evolution of radioactive waste repositories in clay (Yang *et al*., 2008a; Mont *et al*., 2017) and granite (Yang *et al.*, 2007; Samper *et al*., 2008c, Samper *et al*., 2016), analyze stochastic transport and multicomponent competitive cation exchange in aquifers (Samper and Yang, 2006) and study concrete degradation (Galíndez *et al*., 2006). The main applications of INVERSE-FADES-CORE include: the THC and THCM models of the FEBEX in situ test (Samper *et al*., 2008a; Zheng *et al*., 2011; Samper *et al*., 2018); the THCM model of the FEBEX mock up test (Zheng and Samper, 2008); the THCM model of a heating and hydration lab experiment performed on compacted FEBEX bentonite (Zheng *et al*., 2010); and the THC model of the Ventilation Experiment on Opalinus Clay (Zheng *et al*., 2008b).

4 Model results

4.1 Thermal and hydrodynamic results

The injected water saturates the concrete sample in less than 7 days. Later, the water content of the bentonite increases due to the water flow through the concrete. The volumetric water content in the bentonite near the concrete reaches a maximum of 0.5 at 7 days. The volumetric water content of the bentonite near the heater, however, decreases to 0.1 due to water evaporation. Figure 3 shows the spatial distribution of the computed and measured volumetric water content and porosity at the end of the test (t = 1610 days). The computed water content at 1610 days fits the general trend of the measured data. However, it is slightly smaller than the measured values in the bentonite near the B-CI while the computed water content near the heater is larger than the measured values.

The porosity of the bentonite near B-CI increases due to bentonite swelling while it decreases slightly near the heater. In general, the computed porosity in the bentonite reproduces the measured data.

The time evolution of the computed and measured temperature and relative humidity at the two sensors of the HB4 column test are shown in Figure 4. The computed temperatures, which reach steady-state values in a few minutes, reproduce well the measured data at the sensors. The computed relative humidity reproduces the measured data in sensor 1 located near the hydration boundary, but the computed humidity in sensor 2 located near the heater underpredicts the measured relative humidity data. The discrepancies in sensor 2 could be due to an experimental artefact because vapour could have leaked through the sensor hole.

The computed temperature after 2 days of cooling is 25ºC at the hydration boundary (x = 0), 35ºC in the B-CI (x = 0.03 m) and 90ºC near the heater (x = 0.01015 m) (see Figure 1S in Supplementary Material). The computed temperatures at the end of the test reproduce the measured values in the two sensors. The relative humidity in the concrete is 100%. Half of the bentonite sample has a relative humidity almost equal to 100%. The humidity decreases towards the heater interface where the humidity is equal to the initial relative humidity. The computed relative humidity fits the measured values after cooling (Figure 1S in Supplementary Material).

4.2 Chemical results

The calibration of the THCM model of the HB4 was performed with the trial-and-error method by comparing model results with the experimental mineral observations in the concrete and the bentonite at the end of the test, which are listed in Table 1.

The measured aqueous species concentrations were not taken into account for model calibration because inferring the dissolved concentration for reactive species requires a dedicated geochemical modelling based on mineralogical data (Bradbury and Baeyens, 1997, 1998, 2003; Pearson *et al.*, 2003; Zheng *et al.*, 2008a).

4.2.1 pH

Figure 5 shows the spatial distribution of the computed pH at selected times. The initial pH is 12.7 in the concrete and 7.7 in the bentonite. The pH in the bentonite decreases during the first 7 days when calcite precipitates due to the increase in temperature. Then, the pH increases when calcite dissolves. The pH in the concrete decreases due to the diffusion of the alkaline plume into the bentonite. The decrease of the pH is sharp at the B-CI due to the precipitation of brucite in the concrete and calcite and sepiolite in the bentonite. The alkaline front enters the bentonite and moves inside it. The pH front (pH > 8.5) reaches 1.05 cm into the bentonite after the cooling phase. The final pH in the concrete near the hydration boundary (x = 0) is 12.4 and in the bentonite near B-CI (x = 0.03 m) is 11.03. The pH drops from 11.03 to 8.2 in the interval 0.03 < x < 0.044 cm and is slightly larger in the middle of the bentonite sample.

4.2.2 Dissolved species

Figures 6 and 7 show the time evolution of the concentrations of the dissolved Cl^-, Ca^{2+}, Mg^{2+}, Na^+, K^+, HCO_3^-, SO_4^{2-}, Al^{3+} and SiO_2(aq) at two points located 0.5 cm from the B-CI. The point in the concrete is at x = 0.025 m while the point in the bentonite is at x = 0.035 m. These points were selected to illustrate the mass transfer and chemical reactions occurring at both sides of the B-CI.

The computed Cl^- concentration in the concrete increases with time while it decreases in the bentonite due to solute diffusion from the bentonite into the concrete. The computed concentration of Cl^- reaches steady values in the B-CI after 300 days.

The concentration of Na^+ in the concrete increases initially because the concentration of Na^+ in the hydration water is larger than that in the concrete. Then, the concentration of Na^+ decreases in the concrete and the bentonite due to Na^+ exchange with Mg^{2+} in the bentonite.

The concentration of dissolved K^+ in the concrete decreases due to K^+ diffusion from the concrete into the bentonite. The concentration of dissolved K^+ in the bentonite increases during the first 100 days due to the K^+ diffusion from the concrete. Then, the concentration of dissolved K^+ in the bentonite decreases while the concentration of exchanged K^+ increases due to cation exchange.

The concentration of dissolved Mg^{2+} in the concrete increases due to Mg^{2+} diffusion from the bentonite and because the concentration of Mg^{2+} in the hydration water is larger than the initial concentration of the concrete porewater. The diffusion of Mg^{2+} is retarded by brucite and sepiolite precipitation, which is a sink of dissolved Mg^{2+}. The concentration of dissolved Mg^{2+} in the bentonite (x = 0.035 m) decreases due to brucite and sepiolite precipitation and Mg^{2+} diffusion from the bentonite into the concrete. Mg^{2+} undergoes cation exchange in the bentonite near the B-CI.

The concentration of dissolved Ca^{2+} in the concrete increases during the first 50 days due to calcite and portlandite dissolution (Fig. 2S). Later, the concentration drops for a short period of time and then, it keeps increasing. The concentration of dissolved Ca^{2+} in the bentonite decreases due to the thermally-induced precipitation of gypsum and calcite and cation exchange reactions (Fig. 3S). Dissolved Ca^{2+} exchanges mostly with exchanged Mg^{2+}.

The time evolution of the concentration of dissolved HCO_3^- is controlled by calcite dissolution/precipitation and pH. The concentration of HCO_3^- in the concrete increases from its initial value of $1.7 \cdot 10^{-5}$ (see Table 7) to 10^{-4} due to calcite dissolution. Later, it decreases because of calcite precipitation when the concentration of dissolved Ca^{2+} increases due to portlandite dissolution. The concentration of HCO_3^- reaches a stable value after 100 days. The concentration of dissolved HCO_3^- in the bentonite decreases in this location due to calcite precipitation.

The concentration of dissolved SO_4^{2-} in the concrete increases slightly when ettringite dissolves. The concentration increases also because the concentration of SO_4^{2-} in the injected water is larger than the SO_4^{2-} concentration in the concrete porewater. The concentration of dissolved SO_4^{2-} in the bentonite increases due to gypsum dissolution.

The concentration of dissolved Al^{3+} in the concrete decreases initially due to the diffusion from the concrete into the bentonite. Then, it increases slightly when ettringite dissolves. The concentration of Al^{3+} in the bentonite increases slightly due to the diffusion of Al^{3+} from the concrete. An additional source of Al^{3+} is needed to reproduce the observed precipitation of ettringite at the B-CI. The dissolution of the smectite of the bentonite should provide such a source of Al^{3+}.

The concentration of dissolved SiO_2(aq) in the concrete increases due to the dissolution of C1.8SH and because the concentration of dissolved SiO_2(aq) in the hydration water is larger than the initial SiO_2(aq) concentration in the concrete porewater. The concentration of dissolved SiO_2(aq) in the bentonite which is much smaller than the concentration of SiO_2(aq) in the concrete increases due to cristobalite dissolution and the diffusion SiO_2(aq) from the concrete into bentonite.

In summary, the main patterns of the dissolved species are: 1) Dissolved Cl^- and Mg^{2+} diffuse from the bentonite into the concrete; 2) Dissolved K^+, Al^{3+} and SiO_2(aq) diffuse from the concrete into the bentonite; 3) The concentrations of dissolved Na^+, Mg^{2+}, SO_4^{2-} and SiO_2(aq) in the concrete increase initially because their concentrations in the hydration water are larger than those in the concrete; 4) The concentrations of dissolved Na^+, K^+ and Ca^{2+} in the bentonite decrease due to cation exchange with Mg^{2+}; 5) The concentration of dissolved Mg^{2+} in the bentonite decreases due to brucite and sepiolite precipitation, Mg^{2+} diffusion from the bentonite into the concrete and Mg^{2+} exchange; 6) The concentration of dissolved Ca^{2+} in the concrete increases due to portlandite dissolution; 7) The concentration of dissolved Ca^{2+} in the bentonite decreases

due to the thermally-induced precipitation of gypsum and calcite and cation exchange reactions; 8) The concentration of dissolved SO_4^{2-} in the concrete increases slightly when ettringite dissolves while the concentration of SO_4^{2-} in the bentonite increases due to gypsum dissolution; 9) The concentration of dissolved SiO_2(aq) in the concrete increases due to the dissolution of C1.8SH and the concentration of dissolved SiO_2(aq) in the bentonite increases due to cristobalite dissolution.

4.2.3 Minerals

Figure 8 shows the spatial distribution of the computed cumulative dissolution/precipitation of calcite, brucite and cristobalite at t = 1612 days (after 2 days of cooling).

Cristobalite is the silica mineral present initially in the bentonite with an initial concentration of 0.279 mol/kg. Its spatial distribution in the bentonite shows some dissolution due to the increase in temperature that is more pronounced near the heater. Calcite is initially present in the concrete and in the bentonite with concentrations equal to 0.0122 and 0.0584 mol/kg, respectively. Calcite precipitates slightly in the concrete near the hydration zone because the concentration of dissolved Ca^{2+} in the hydration water is larger than that of the initial concrete porewater. Calcite precipitates at both sides of the B-CI, being large in the bentonite concrete near the B-CI (maximum value of 1.17 mol/kg) at 1610 days, while portlandite and C1.8SH dissolve. The precipitation front of calcite penetrates 0.44 cm into the bentonite and 0.06 cm into the concrete at t = 1612 days. It can be seen a dissolution front of calcite in the bentonite which advances with time.

Brucite is initially present in the concrete with a concentration of 0.1834 mol/kg. This mineral precipitates near the hydration boundary in the first 0.1 cm of the concrete because the concentration of dissolved Mg^{2+} in the hydration water is larger than that of

the initial concrete porewater. Brucite precipitates also in the concrete and bentonite near the B-CI. The peak of precipitation is located in the concrete with a maximum concentration of 4.3 mol/kg at t =1610 days. The front of brucite precipitation spreads 0.12 cm into concrete and 0.47 cm into bentonite at t = 1610 days (Figure 8).

Ettringite is initially present only in the concrete with a concentration of 0.0139 mol/kg. A very small amount of ettringite precipitates near the hydration boundary and dissolves in the rest of the concrete (not shown here). Ettringite dissolution is largest near the B-CI.

Figure 8 shows the spatial distribution of the computed cumulative dissolution/precipitation of sepiolite, gypsum, portlandite and C1.8SH at t = 1612 days (after 2 days of cooling).

Sepiolite is a secondary mineral which precipitates in narrow bands at both sides of the B-CI of 0.59 cm in the bentonite and 0.03 cm in the concrete.

Gypsum is only present initially in the bentonite. Its initial concentration is equal to 0.00673 mol/kg. Anhydrite is a secondary mineral. Gypsum dissolves initially because the initial bentonite water is not in equilibrium with gypsum. Gypsum precipitates in the bentonite near the B-CI from t = 7 to t = 30 days. A precipitation front of anhydrite starts in the bentonite at t = 7 days. The front moves towards the heater. All the precipitated anhydrite dissolves after 1000 days (Figure 4S).

Portlandite is initially present only in the concrete with an initial concentration of 1.01 mol/kg. This mineral dissolves uninterruptedly in all the concrete, especially near the B-CI. The maximum cumulative dissolution of portlandite after the cooling phase in the concrete near the B-CI is 0.048 mol/kg.

C1.8SH is present initially only in the concrete with an initial concentration of 0.366 mol/kg while C0.8SH is a secondary mineral. C1.8SH dissolves in the concrete, except

near the hydration boundary (about x < 0.015 m) where it precipitates because the SiO_2(aq) and Ca^{2+} concentrations in the boundary water are larger than those of the concrete porewater. The largest dissolution occurs in the concrete near the B-CI. C0.8SH precipitates in the concrete in extremely small amounts (10^{-11} mol/kg near the hydration boundary and 10^{-12} mol/kg near the B-CI). Quartz is the main mineral component of the concrete with an initial volume fraction of 62.2%. Its dissolution is not relevant (2.5 10^{-10} mol/kg). Anorthite is a secondary mineral, which does not precipitate.

Figure 5S shows the spatial distribution of the initial and final (t = 1612 days, after 2 days of cooling) mineral volume fractions. The most abundant minerals initially in the concrete are quartz, C1.8SH and portlandite. The more relevant mineral in the bentonite is smectite which is not considered as a reactive mineral in the model because smectite dissolution is considered to be too slow in the short-term geochemical model of the HB4 column test. The main changes in mineral volume fractions are the increase of the brucite volume fraction near the hydration boundary and in the concrete near the B-CI and the reduction of the volume fraction of C1.8SH and portlandite. The most important change in the bentonite is the increase of the calcite volume fraction near the B-CI.

4.2.4 Changes in porosity

The numerical model assumes that the porosities are constant in time. The changes in porosity due to mineral dissolution/precipitation have been evaluated from the computed mineral volume fractions. Figure 9 shows the spatial distribution of the porosity at the end of the HB4 column test. The final porosity differs from the initial porosity mostly in: 1) The hydration boundary, 2) The concrete near the B-CI, and 3) The bentonite near the B-CI. The porosity in the hydration zone decreases 48% mainly due to brucite precipitation. Other minerals such as calcite, ettringite, C1.8SH and C0.8SH also precipitate in this zone and contribute to the porosity decreasing, but at a much smaller rate. The porosity in the interval 0.015 m < x < 0.029 m increases about 6.5% due to the

combined effect of C1.8SH, portlandite and ettringite dissolution in the concrete. The porosity reduces to zero in a 0.03 cm thick zone in the concrete near the B-CI due to brucite and calcite precipitation. The porosity of the bentonite near the B-CI decreases about 22% due to the precipitation of brucite, calcite and sepiolite. The porosity in the central zone of the bentonite increases slightly (1.5%) due to calcite dissolution.

4.2.5 Cation exchange and surface complexation

Cation exchange and surface complexation reactions take place only in the bentonite.

The precipitation of brucite in the bentonite near the B-CI depletes the concentration of dissolved Mg^{2+}, which causes the exchange of the Mg^{2+} in the bentonite interlayers with the remaining cations, especially with dissolved Ca^{2+} and Na^{+}. The computed concentrations of exchanged Ca^{2+} and Na^{+} in the bentonite near the B-CI are larger than the initial concentrations (Figure 10). On the other hand, the concentration of exchanged Mg^{2+} near the B-CI is smaller than the concentration in the rest of the bentonite sample. The computed concentration of exchanged K^{+} in the bentonite near the B-CI increases initially and then decreases with time.

The computed concentrations of Ca^{2+}, Na^{+} and K^{+} reproduce well the measured exchanged data. Model results of exchanged Mg^{2+} reproduce the general trend of the measured data, but show significant deviations from measured data, possibly due to the uncertainties in the Mg mineral phases forming at the B-CI.

The spatial distribution of the computed concentrations of sorbed species at t = 1610 days is shown in Figure 6S. The predominant surface complexes in the bentonite near the B-CI are S^{s}-O^{-}, S^{w1}-O^{-} and S^{w2}-O^{-}. The bentonite zone where the surface complexes are affected by the concrete interactions at t = 1061 days is about 3 cm thick.

4.3 Sensitivity analysis

Some of the uncertainties of the THCM model have been quantified with a sensitivity analysis to: 1) The grid size; 2) The temperature of the test (non-isothermal versus a constant and uniform temperature of 25ºC); and 3) The specific surface for the kinetic dissolution/precipitation of ettringite.

The grid size in the base run is non-uniform with a minimum grid size of 0.01 cm at the B-CI. Several sensitivity runs were performed with uniform grids having grid sizes of 0.09, 0.045 and 0.018 cm. Mineral precipitation and the thickness of the zone affected by mineral precipitation in the bentonite near the B-CI increase when the grid size increases (see Figure 7S). On the other hand, pore clogging in the concrete near the B-CI is computed for grid sizes smaller than 0.018 cm.

A sensitivity run was performed at a constant and uniform temperature of 25ºC. The peaks of brucite and calcite precipitation for constant temperature are smaller than those of the base run (Figure 8 S). Moreover, the thickness of the bentonite zone with calcite and brucite precipitation in the constant temperature run is larger than that of the base run. Brucite precipitates in the concrete and in the bentonite in the base run while brucite precipitates only in the bentonite in the constant temperature run. The reduction in porosity in the concrete near the B-CI in the constant temperature run is smaller than that of the base run (Figure 9 S). The results of the sensitivity run to isothermal conditions attest the conclusions of the experimental study of Lalan *et al*. (2016) which showed that the temperature plays an important role in the degradation of CSH and the precipitation of mineral phases.

The discrepancies of the model predictions for kinetically-controlled ettringite precipitation could be related to the uncertainties in its specific surface. A sensitivity run was performed by increasing the specific surface of ettringite by a factor of 10 (see Figure

10S). The increase of the specific surface leads to more precipitation of this mineral in the mid upstream part of the concrete sample, more ettringite dissolution in the concrete near the B-CI and a smaller penetration of the pH front into the bentonite. The results of the sensitivity run tend to favour an increase in the specific surface of ettringite. However, the discrepancies in the concrete near the B-CI still persist.

5 Comparison of model results and experimental mineralogical data

Table 1 shows a summary of the main computed and experimental observations of minerals at the end of the HB4 column test. For the most part, the numerical model captures the main trends of mineral dissolution/precipitation, including: 1) Calcite and brucite precipitation in the concrete near the hydration boundary; 2) Portlandite dissolution and calcite and ettringite precipitation in the central zone of the concrete sample; 3) Calcite precipitation in the concrete near the bentonite interface; 4) Calcite and sepiolite precipitation in the bentonite near the concrete interface and lack of ettringite and anorthite precipitation; 5) Calcite dissolution in the bentonite far from the B-CI; and 6) Gypsum precipitation in the bentonite near the heater.

However, there are some discrepancies for ettringite and CSH. The numerical model predicts much less precipitation than the observed values for these phases. The model does not reproduce the observed precipitation of ettringite at the B-CI probably because an additional source of Al^{3+} is needed. The dissolution of the smectite of the bentonite would provide such a source of Al^{3+}. The deviations on CSH precipitation could be related to uncertainties in the selection of the appropriate CSH, CASH and MSH phases.

The model predicts the precipitation of sepiolite and brucite in the bentonite near the B-CI while the experimental observations detected Mg-silicates such as sepiolite and

saponite. This discrepancy could be overcome by accounting for smectite dissolution and saponite precipitation.

6 Conclusions

A fully coupled thermo-hydro-chemical-mechanical model of the heating and hydration concrete-bentonite column test has been presented. Experimental observations indicate that calcite and brucite precipitated in the concrete near the hydration boundary, portlandite dissolved and calcite and ettringite precipitated in the concrete, calcite and sepiolite precipitated in the bentonite near the B-CI, calcite dissolved in the bentonite far from the B-CI and gypsum precipitated in the bentonite near the heater.

The computed temperatures reach steady state in a few minutes. The bentonite hydrates through the concrete sample, which gets fully saturated after 7 days. The computed water content in the bentonite near the B-CI increases to 0.5 due to the hydration and decreases to 0.1 near the heater due to water evaporation. The computed relative humidities increase and reach steady state after 250 days with RH = 100% at the sensor located near the hydration boundary and RH = 40% near the heater. The computed porosity of the bentonite near the concrete increases 25% due to bentonite swelling and decreases 10% near the heater due to the bentonite drying.

Model results show that advection is relevant during the first months of the test. Then, solute diffusion is the main transport mechanism. The differences in the chemical composition of the initial and boundary waters cause diffusion fronts. Dissolved Cl^- and Mg^{2+} diffuse from the bentonite into the concrete while dissolved K^+, Al^{3+} and SiO_2(aq) diffuse from the concrete into the bentonite. The concentrations of dissolved Na^+, Mg^{2+}, SO_4^{2-} and SiO_2(aq) in the concrete increase initially because their concentrations in the hydration water are larger than those in the concrete.

The thermal field induces calcite and gypsum precipitation and a decrease of pH in the bentonite. Later, calcite and gypsum dissolve in the central zone of the bentonite. Cation exchange reactions play a major role in the bentonite, especially near the B-CI where dissolved Na^+, K^+ and Ca^{2+} exchange with Mg^{2+}. The main mineralogical alterations are predicted to occur at the hydration boundary and at both sides of the B-CI. Calcite and brucite precipitate in the concrete near the hydration boundary because the concentrations of bicarbonate and magnesium in the hydration water are larger than their respective initial concentrations. Calcite and brucite precipitate in the bentonite and the concrete, especially near the B-CI. Sepiolite also precipitates in the concrete and bentonite near the B-CI. The model predicts the dissolution of portlandite and C1.8SH in the concrete and a very small precipitation of C0.8SH. Ettringite precipitates in the concrete near the hydration boundary and dissolves in the rest of the concrete, but at very small rates.

The most important changes in the porosity in the HB4 column test occur in the hydration boundary and at the B-CI. The porosity in the hydration boundary decreases when brucite precipitates. Calcite, ettringite, C1.8SH and C0.8SH precipitation also contribute to the decrease in the porosity. Their contributions, however, are much smaller than that of brucite. The porosity in the concrete near the B-CI reduces 100% due to brucite and calcite precipitation. The porosity in the bentonite near the B-CI decreases 22% when brucite, calcite and sepiolite precipitate.

The computed pH shows a sharp decrease at the B-CI which coincides with the precipitation of brucite in the concrete and calcite and sepiolite in the bentonite. The alkaline front penetrates and migrates through the bentonite. The pH front (pH > 8.5) reaches 1 cm into the bentonite after the cooling phase.

Model results are sensitive to grid size. Mineral precipitation and the thickness of the zone affected by mineral precipitation in the bentonite near the B-CI increase when

the grid size increases while pore clogging in the concrete near the B-CI is computed only for grid sizes smaller than 0.018 cm. The non-isothermal conditions play an important role in the precipitation of mineral phases. The reduction in porosity in the B-CI for constant temperature is smaller than that of the non-isothermal run. An increase of the specific surface of ettringite by a factor of 10 leads to more precipitation of this mineral in the mid upstream part of the concrete sample, more ettringite dissolution in the concrete near the B-CI and a smaller penetration of the pH front into the bentonite.

The model reproduces the measured temperature, relative humidity, water content and porosity data. However, the model overestimates the relative humidity measured at the sensor near the heater. The model captures the main trends of the geochemical interactions and mineralogical transformations taking place at the B-CI. However, the model shows discrepancies for exchanged Mg^{2+} because there are uncertainties in the Mg mineral phases forming at the B-CI (Dauzères *et al*., 2016). The model does not reproduce the observed precipitation of ettringite at the B-CI probably because an additional source of Al^{3+} is needed. The dissolution of the smectite of the bentonite would provide such a source of Al^{3+}. The model presented in this paper does not account for smectite dissolution in the bentonite because the rate of this reaction is supposed to be small enough for it to be relevant in the geochemical model of the HB4 column test. The long-term model predictions of Marty *et al*. (2009) show that the dissolution of illite, kaolinite and montmorillonite, which are the main sources of soluble Al species, will favour the precipitation of CASH phases and ettringite in the concrete. The precipitation of these phases in short-term tests, however, is not expected to be relevant due to the limited extent of montmorillonite dissolution (Soler, 2013). Samper *et al*. (2018) analyzed the relevance of smectite dissolution in the FEBEX in situ test. They reported model results with and without kinetic smectite dissolution. The computed concentration of dissolved aluminum with smectite dissolution is significantly larger than that computed without smectite

dissolution, the concentrations of dissolved cations increase slightly while the concentrations of anions and neutral species lack sensitivity to smectite dissolution. The model of the HB4 column test presented here could be improved by accounting for smectite dissolution and other mineral phases such as CASH, MSH and other Mg silicates.

Although the model results improve with the increase in the specific surface of ettringite, the discrepancies in CSH and ettringite in the concrete near the B-CI still persist.

The model of the HB4 column test presented here does not consider the changes in porosity due to chemical reactions. Samper *et al.* (2017) and Águila *et al.* (2018) evaluated the effect of the porosity changes of the interactions of concrete, compacted bentonite and clay in a HLW repository in clay with a reactive transport model. Their results indicate that there are significant differences in the mineral dissolution/precipitation computed with and without the feedback effect. The thickness of pore clogging in the concrete and at the concrete-clay interface computed with the porosity feedback is smaller than that computed without the porosity feedback. Future models of the HB4 column test could be improved by considering the effect of porosity changes due to chemical reactions and by using inverse methods to calibrate model parameters in a manner similar to Yang *et al*. (2008b; 2014).

Although solid solution models such as those reported by Soler (2013) and Savage *et al.* (2011) are required to quantify the chemical evolution of CSH, AFm and ettringite during the early phases of concrete hydration (Kulik and Kersten, 2011; Lothenbach and Winnefeld, 2006), the dominant reactions for the conditions of the HB4 column test are portlandite dissolution and the decalcification of C1.8SH to form C0.8SH in the concrete-bentonite clay interface. These reactions have been identified experimentally and are corroborated by model results.

FEBEX bentonite behaves mostly as a mixed mono(Na)-divalent (Ca,Mg)-exchanged montmorillonite and the mixed Ca-Na-exchange displacement of Mg is not expected to produce important changes in the swelling properties of the bentonite.

7 Acknowledgements

The research leading to these results has received funding from the European Union's European Atomic Energy Community's (Euratom) Horizon 2020 Programme (NFRP-2014/2015) under grant agreement, 662147 – CEBAMA. This work was partly funded by the Spanish Ministry of Economy and Competitiveness (Project CGL2016-78281) with support from the FEDER funds and the Galician Regional Government (Ref: ED431C 2017/67 from "Consolidación e estruturación de unidades de investigación competitivas", Grupos de referencia competitiva). The second author enjoyed a research contract from University of A Coruña. We thank the comments, corrections and suggestions of the Guest Editor and the two anonymous reviewers who contributed to the improvement of the paper.

8 References

Águila J, J Samper & A Mon. 2018. CORE^{2D}V5: A reactive transport code for the dynamic update of the flow, transport and chemical parameters, submitted to Computer and Geosciences.

Alonso, M.C., García, J. L., Cuevas, J., Turrero, M.J., Fernández, R., Torres, E., Ruiz, A.I., 2017. Interaction processes at the concrete-bentonite interface after 13 years of FEBEX Plug operation. Part I: Concrete alteration, Physics and Chemistry of the Earth, Parts A/B/C, 99, 38-48.

Ayora, C., Soler, J. M., Saaltink, M. W., Carrera, J., 2007. Modelo de transporte reactivo sobre la lixiviación del hormigón por agua subterránea en la Celda 16 de El Cabril. Techn. Publ. ENRESA PT 05-2007.

Balmer, S., Kaufhold, S., Dohrmann, R., 2017. Cement-bentonite-iron interactions on small scale tests for testing performance of bentonites as a barrier in high-level radioactive waste repository concepts. Applied Clay Science 135, 427–436.

Berner, U., Kulik, D. A., Kosakowski, G., 2013. Geochemical impact of a low-pH cement liner on the near field of a repository for spent fuel and high-level radioactive waste. Physics and Chemistry of the Earth 64, 46-56.

Bradbury, M.H., Baeyens, B., 1997. A mechanistic description of Ni and Zn sorption on Na-montmorillonite. Part II: modelling. J. Contam. Hydrol. 27, 223–248.

Bradbury, M.H., Baeyens, B., 1998. A physicochemical characterisation and geochemical modelling approach for determining pore water chemistries in argillaceous rocks. Geochim. Cosmochim. Acta 62, 783–795.

Bradbury, B., Baeyens, B., 2003. Pore water chemistry in compacted resaturated MX-80 bentonite. J. Contam. Hydrol. 61, 329–338.

Cuevas J., A. I. Ruiz, R. Fernández, E. Torres, A. Escribano, M. Regadío, M.J. Turrero. 2016. Lime mortar-compacted bentonite-magnetite interfaces: An experimental study focused on the understanding of the EBS long-term performance for high-level waste isolation DGR concept. Applied Clay Science 124-125, 79-93.

Dai, Z., Samper, J., 2004. Inverse problem of multicomponent reactive chemical transport in porous media: formulation and applications. Water Resour Res 40, W07407.

Dai, Z., Samper, J., 2006. Inverse modeling of water flow and multicomponent reactive transport in coastal aquifer systems. J. Hydrol. 327 (3-4), 447–461.

Dai, Z., Samper, J., Ritzi, R., 2006. Identifying geochemical processes by inverse modeling of multicomponent reactive transport in Aquia aquifer. Geosphere 4 (4), 210–219.

Dauzères A., G. Achiedo, D. Nied, E. Bernard, S. Alahrache, B. Lothenbach. 2016. Magnesium perturbation in low-pH concretes placed in clayey environment solid characterizations and modeling. Cement and Concrete Research 79, 137-150.

Drever L.L., 1998. The Geochemistry of Natural Waters. Prentice Hall, New Jersey.

De Windt, L., Pellegrini, D., van der Lee, J., 2004. Coupled modeling of cement/claystone interactions and radionuclide migration. J. Contam. Hydrol. 68, 165-182.

De Windt L., F. Marsa, E. Tinseau, D. Pellegrini. 2016. Reactive transport modeling of geochemical interactions at a concrete/argillite interface, Tournemire site (France). Physics and Chemistry of the Earth 33, S295-S305.

ENRESA 2000. FEBEX Project. Full-scale engineered barriers experiment for a deep geological repository for high-level radioactive waste in crystalline host rock. Final Report. Publicación Técnica ENRESA 1/2000, Madrid, 354 pp.

ENRESA 2004. Evaluación del comportamiento y de la seguridad de un almacén geológico profundo de residuos radiactivos en arcilla. PT 49-1PP-M-A1-01. [in Spanish]

ENRESA, 2006a. Full-Scale Engineered Barriers Experiment: Updated Final Report. ENRESA Tech. Publ. PT 05-02/2006, 589 pp.

ENRESA, 2006b. FEBEX : Final THG Modelling Report. ENRESA Tech. Publ. PT 05-03/2006, 155 pp.

Fernández A.M., Cuevas, J. and Rivas, P., 2001. Pore water chemistry of the FEBEX bentonite. Mat. Res. Soc. Symp. Proc. 663,573-588.

Fernández A.M., Baeyens, B., Bradbury, M. and Rivas, P., 2004. Analysis of pore water chemical composition of a Spanish compacted bentonite used in an engineered barrier. Phys. Chem Earth (29), 105-118.

Fernández, R., Cuevas, J., Mäder, U.K., 2009a. Modelling concrete interaction with a bentonite barrier. Eur. J. Mineral 21, 177-191.

Fernández, R., Mäder, U.K., Rodriguez, M., Vigil de la Villa, R., Cuevas, J., 2009b. Alteration of compacted bentonite by diffusion of highly alkaline solutions. Eur. J. Mineral. 21, 725–735.

Fernández, R., Torres, E., Ruiz, A. I., Cuevas, J., Alonso, M. C., García, J. L., Rodríguez, E., Turrero, M. J., 2017. Interaction processes at the concrete-bentonite interface after 13 years of FEBEX-Plug operation. Part II: Bentonite contact. Physics and Chemistry of the Earth, Parts A/B/C, 99, 49-63.

Gaucher E. and P. Blanc, 2006, Cement/clay interactions – A review: Experiments, natural analogues, and modeling, Waste Management, 26(7): 776-788.

Galíndez, J.M., Molinero, J., Samper, J., Yang, C.B., 2006. Simulating concrete degradation processes by reactive transport models. J. Phys. IV France 136, 177–188.

Hunt, G., Ghanbarian, B., Skinner, T. E. and Ewing, R. P., 2015. Scaling of geochemical reaction rates via advective solute transport. CHAOS: An interdisciplinar Journal of nonlinear science. 25, 075403. doi : http://dx.doi.org/10.1063/1.4913257

Kosakowski, G., Berner, U., 2013. The evolution of clay rock/cement interfaces in a cementitious repository for low- and intermediate level radioactive waste. Physics and Chemistry of the Earth 64, 65-86.

Kulik, D.A. & Kersten, M., 2001. Aqueous solubility diagrams for cementitious waste stabilization systems: II, end-member stoichiometries of ideal calcium silicate hydrate solid solutions. J. Am. Ceram. Soc. 84, 3017–3026.

Lalan P., A. Dauzères, L. DeWindt, D. Bartier, J. Sammaljärvi, J.D. Barnichon, I. Techer, V. Detilleux. 2016. Impact of a 70 °C temperature on an ordinary Portland cement paste/claystone interface: An in situ experiment. Cement and Concrete Research 83, 164-178.

Lloret, A., Alonso, E.E., 1995. State surfaces for partially saturated soils. In: Proceedings of the International Conference on Soils Mechanics and Foundation Engineering, Balkema, pp. 557–562.

Lothenbach, B. & Winnefeld, F., 2006. Thermodynamic modelling of the hydration of Portland cement. Cem. Concr. Res. 36, 209–226.

Lothenbach, B., Bernard and E., Mäder, U., 2017. Zeolite formation in the presence of cement hydrates and albite. Physics and Chemistry of the Earth, 99, 77-94.

Marty, N.C.M., Tournassat, C., Burnol, A., Giffaut, E., Gaucher, E. C., 2009. Influence of reaction kinetics and mesh refinement on the numerical modelling of concrete/clay interactions. Journal of Hydrology 364, 58-72.

Marty N. C. M, O. Bildstein, P. Blanc, F. Claret, B. Cochepin, E. C. Gauchern, D. Jacques, J.-E. Lartigue, S. Liu, K. U. Mayer, J. C. L. Meeussen, I. Munier, I. Pointeau, D. Su, C.I. Steefel. 2015. Benchmarks for multicomponent reactive transport across a cement/clay interface. Comput. Geoscience 19, 635-653.

Melkior, T., D. Mourzagha, S. Yahiaouia, D. Thobya, J. C. Alberto, C. Brouard, N. Michau, 2004, Diffusion of an alkaline fluid through clayey barriers and its effect on the diffusion properties of some chemical species, Applied Clay Science, Vol. 26, Issues 1–4, 99-107

Molinero, J., Samper, J., Zhang, G., Yang, C., 2004. Biogeochemical reactive transport model of the redox zone experiment of the Äspö hard rock laboratory in Sweden. Nucl. Technol. 148, 151–165.

Molinero, J., Samper, J., 2006. Modeling of reactive solute transport in fracture zone of granitic bedrocks. J. Cont. Hydrol. 82, 293–318.

Mon, A, 2017. Coupled thermo-hydro-chemical-mechanical models for the bentonite barrier in a radioactive waste repository. Ph. D. Dissertation. Universidad de A Coruña, Spain.

Mon, A., Samper, J., Montenegro, L., Naves, A., Fernández, J., 2017. Reactive transport model of compacted bentonite, concrete and corrosion products in a HLW repository in clay. Journal of Contaminant Hydrology 197, 1-16.

Navarro, V., 1997. Modelo de comportamiento mecánico e hidráulico de suelos no saturados en condiciones no isotermas. Ph.D. Dissertation, Universidad Politécnica de Cataluña, 329 pp.

Navarro, V. and Alonso, E.E., 2000. Modelling swelling soils for disposal barriers. Compt. Geotech. 27,19-43.

Nguyen, T.S., Selvadurai, A.P.S., Armand, G., 2005. Modelling the FEBEX THM experiment using a state surface approach. Int. J. Rock Mech. Min. Sci. 42 (5–6), 639–651.

Pearson, F.J., Arcos, D., Bath, A., Boisson, J.-Y., Fernández, A.M., Gäbler, H.-E., Gaucher, E., Gautschi, A., Griffault, L., Hernán, P., Waber, H.N., 2003. Mont Terri Project – Geochemistry of water in the Opalinus Clay Formation at the Mont Terri Rock Laboratory. Swiss Federal Office for Water and Geology Series No. 5.

Samper, J., Yang, C., Montenegro, L., 2003. CORE^{2D} version 4: a code for non-isothermal water flow and reactive solute transport. User's Manual. University of La Coruña, Spain.

Samper, J., Dai, Z., Molinero, J., García-Gutiérrez, M., Missana, T., Mingarro, M., 2006. Inverse modeling of tracer experiments in FEBEX compacted Ca-bentonite. Phys. Chem. Earth 31, 640–648.

Samper, J., Yang, C., 2006. Stochastic analysis of transport and multicomponent competitive monovalent cation exchange in aquifers. Geosphere 2 (April), 102–112.

Samper, J., Zheng, L., Montenegro, L., Fernández, A.M., Rivas, P., 2008a. Testing coupled thermo-hydro-chemical models of compacted bentonite after dismantling the FEBEX in situ test. Appl. Geochem. (23/5), 1186–1201.

Samper, J., Zheng, L., Fernández, A.M., Montenegro, L., 2008b. Inverse modeling of multicomponent reactive transport through single and dual porosity media. J.Cont. Hydrol.

Samper, J., C. Lu, & L. Montenegro, 2008c, Reactive transport model of interactions of corrosion products and bentonite Physics and Chemistry of the Earth, Vol. 33, Supplement 1, S306-S316.

Samper, J., T. Xu and C. Yang, 2009, A sequential partly iterative approach for multicomponent reactive transport CORE^{2D}, Comput Geosci, 13:301–316.

Samper, J., Yang, C., Zheng, L., Montenegro, L., Xu, T., Dai, Z., Zhang, G., Lu, C., and Moreira, S., 2011. CORE^{2D} V4: a code for water flow, heat and solute transport, geochemical reactions, and microbial processes. Chapter 7 of the Electronic Book Groundwater Reactive Transport Models. In: Zhang F., Yeh G.-T., Parker C., Shi X. (Eds.) Bentham Science Publishers, pp 161–186.

Samper J, A Naves, L Montenegro & A Mon, 2016, Reactive transport modelling of the long-term interactions of corrosion products and compacted bentonite in a HLW repository in granite: Uncertainties and relevance for performance assessment, Applied Geochemistry. Vol 67 (2016) 42-51.

Samper J., A. Mon, J. Fernández & L. Montenegro. 2017. Discretization errors and porosity feedback for the long-term reactive transport model of the interactions of concrete, compacted bentonite and clay in a HLW repository in clay. In: CEBAMA 2nd Annual Workshop Proceedings, Contribution ST_3.14, 10 pp (in press).

Samper, J, A. Mon & L. Montenegro. 2018. A revisited thermal, hydrodynamic, chemical and mechanical model of compacted bentonite for the entire duration of the FEBEX in situ test, Applied Clay Sciences, doi.org/10.1016/j.clay.2018.02.019.

Savage, D., Benbow, S., Watson, C., Takase, H., Ono, K., Oda, C., Honda, A., 2010. Natural systems evidence for the alteration of clay under alkaline conditions: an example from Searles Lake, California. Applied Clay Science 47, 72–81.

Savage, D., 2011. A review of analogues of alkaline alteration with regard to long-term barrier performance. Mineral. Mag. 75, 2401–2418.

Savage, D., Soler, J.M., Yamaguchi, K., Walker, C., Honda, A., Inagaki, M., Watson, C., Wilson, J., Benbow, S., Gaus, I., Rueedi, J., 2011. A comparative study of the modelling of cement hydration and cement-rock laboratory experiments. Applied Geochemistry 26, 11381152.

Savage, D., 2012. Prospects for coupled modelling. STUK-TR 13. Radiation and Nuclear Safety Authority.

Shao, H., Kosakowski, G., Berner, U., Kulik, D.A., Mäder, U., Kolditz, O., 2013. Reactive transport modeling of the clogging process at Maqarin natural analogue site. Physics and Chemistry of the Earth 64, 21-31.

Soler J.M, J. Samper, A. Yllera, A. Hernández, A. Quejido, M. Fernández, C. Yang, A. Naves, P. Hernán, and P. Wersin, 2008, The DI-B in-situ diffusion experiment at Mont Terri: results and modelling, Physics and Chemistry of the Earth, Vol. 33. Supplement 1, 2008, S196-S207.

Soler J. M., 2013. Reactive transport modeling of concrete-clay interaction during 15 years at the Tournemire Underground Rock Laboratory. European Journal of Mineralogy, 25 935-1221

Steefel, C.I., Lichtner, P.C., 1998. Multicomponent reactive transport in discrete fractures II. Infiltration of hyperalkaline groundwater at Maqarin, Jordan, a natural analogue site. J. Hydrol. 209, 200-224.

Torres E., Turrero M.J., Escribano A., Martín P.L., 2013. Geochemical interactions at the concrete-bentonite interface of column experiments. Deliverable 2.3-6-1 of the PEBS Project. CIEMAT. Madrid.

Turrero, M. J., Villar, M. V., Torres, E., Escribano, A., Cuevas, J., Fernández, R., Ruiz, A. I., Vigil de la Villa, R., del Soto, I., 2011. Deliverable 2.3-3-1 of PEBS Project. Laboratory tests at the interfaces, Final results of the dismantling of the tests FB3 and HB4, 2011. CIEMAT. Madrid.

Villar, M. V., Martín, P. L., Romero, F. J., Gutiérrez-Rodrigo, V., Barcala, J. M., 2012. Gas and Water Permeability of Concrete. Technical Report CIEMAT.

Villar, M. V., 2013. Long-term Performance of Engineered Barrier Systems PEBS. Summary of concrete hydraulic properties determined at CIEMAT. Technical Note CIEMAT/DMA/2G210/01/13.

Watson, C., Hane, K., Savage, D., Benbow, S., Cuevas, J., Fernández, R., 2009. Reaction and diffusion of cementitious water in bentonite: results of 'blind' modelling. Applied Clay Science 45, 54–69.

Watson, C., Savage, D., Wilson, J., Benbow, S., Walker, C., Norris, S., 2013. The Tournemire industrial analogue: reactive transport modelling of a cement-clay interface. Clay Miner. 48, 167-184.

Watson, C., Wilson, J., Savage, D., Benbow, S., Norris, S., 2016. Modelling reactions between alkaline fluids and fractured rock: The Maqarin natural analogue. Applied Clay Science 121-122, 46–56.

White, A.F. and Brantley, S.L., 2003. The effect of time on the weathering rates of silicate minerals. Why do weathering rates differ in the lab and in the field? Chem. Geol. 202, 479-506.

Wollery, T.J., 1992. EQ3/3. A software package for geochemical modeling of aqueous system: package overview and installation guide version 7.0. UCRL-MA-110662-PT-I, Lawrence Livermore National Laboratory, Livermore, California.

Xu, T., Samper, J., Ayora, C., Manzano, M., Custodio, E., 1999. Modeling of non-isothermal multi-component reactive transport in field scale porous media flow systems. J. Hydrol. 214 (1–4), 144–164.

Yamaguchi, T., Sakamoto, Y., Akai, M., Takazawa, M., Iida, Y., Tanaka, T., Nakayama, S., 2007. Experimental and modeling study on long-term alteration of compacted bentonite with alkaline groundwater. Physics and Chemistry of the Earth 32, 298-310.

Yang, C., Samper, J., Molinero, J., Bonilla, M., 2007. Modeling geochemical and microbial consumption of dissolved oxygen after backfilling a high level radioactive waste repository. J. Contam. Hydrol. 93, 130–148.

Yang, C., J. Samper, & L Montenegro 2008a. A coupled non-isothermal reactive transport model for long-term geochemical evolution of a HLW repository in clay. Environmental Geology 53, 1627–1638, doi: 10.1007/s00254-007-0770-2.

Yang, C.; J. Samper, M. Molinero, 2008b. Inverse Microbial and Geochemical Reactive Transport Models in Porous Media. Phys. Chem. Earth 2008, 33 (14-16), 1026-1034.

Yang, C., Z. Dai, K.D. Romanak, S. D. Hovorka, R.H. Treviño, 2014, Inverse Modeling of Water-Rock-CO_2 Batch Experiments: Potential Impacts on Groundwater Resources at Carbon Sequestration Sites. Environ. Sci. Technol, 48 (5), 2798-2806

Zhang, G., Samper, J., Montenegro, L., 2008. Coupled thermo-hydro-bio-geochemical reactive transport model of the CERBERUS heating and radiation experiment in Boom clay. Appl. Geochem. (23/4), 932–949.

Zheng, L., 2006. Coupled thermo-hydro-mechanical-geochemical models for structured deformable porous media. Ph.D. Dissertation, Universidad de A Coruña, A Coruña, Spain, 439 pp.

Zheng, L. and Samper, J., 2008. A coupled THMC model of FEBEX mock-up test. Physics and Chemistry of the Earth 33, S486-S498.

Zheng L and J Samper, 2015, Dual-continuum multicomponent reactive transport with nth-order solute transfer terms for structured porous media, Comp. Geos, Vol. 19(4): 709-726. DOI 10.1007/s10596-015-9477-8.

Zheng, L., Samper, J. and Montenegro, L., 2008a. Inverse hydrochemical model of aqueous test. Physics and Chemistry of the Earth 33,1009-1018

Zheng, L., J. Samper, L. Montenegro & J.C. Mayor, 2008b, Flow and reactive transport model of a ventilation experiment in Opallinus clay, Physics and Chemistry of the Earth, Vol. 33, S486–S498. doi:10.1016/j.pce.2008.05.012

Zheng, L., Samper, J., Montenegro, L. and Fernández, A.M., 2010. A coupled THMC model of a heating and hydration laboratory experiment in unsaturated compacted FEBEX bentonite. Journal of Hydrology 386, 80-94.

Zheng. L, J. Samper and L. Montenegro, 2011, A coupled THC model of the FEBEX in situ test with bentonite swelling and chemical and thermal osmosis, J of Contaminant Hydrology 126:45–60. doi:10.1016/j.jconhyd.2011.06.003

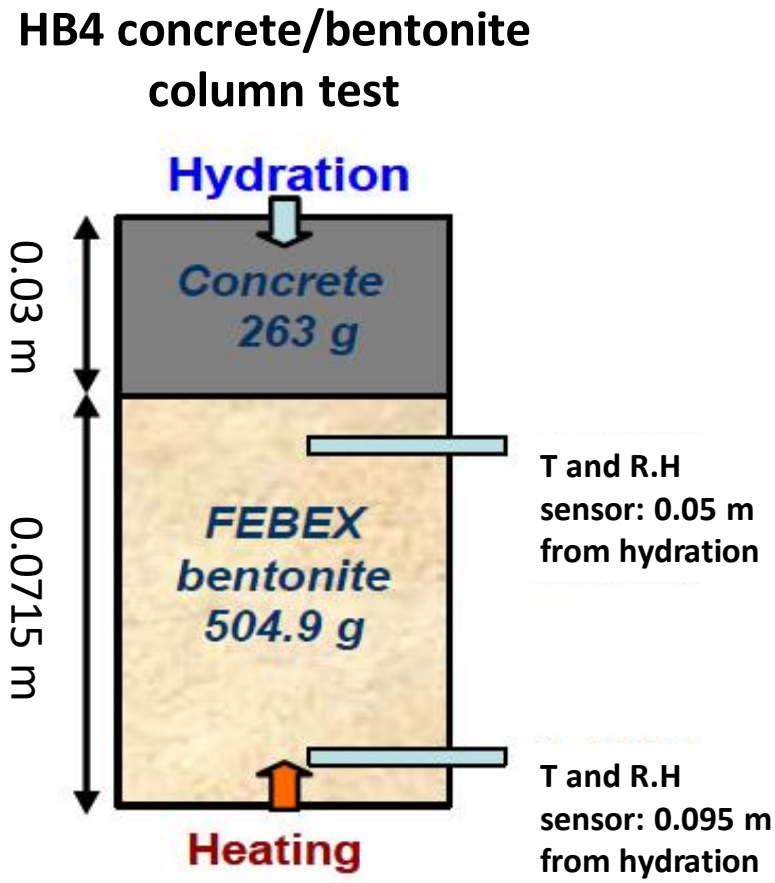

Figure 1. Sketch of the HB4 concrete-bentonite column test (Turrero *et al*., 2011).

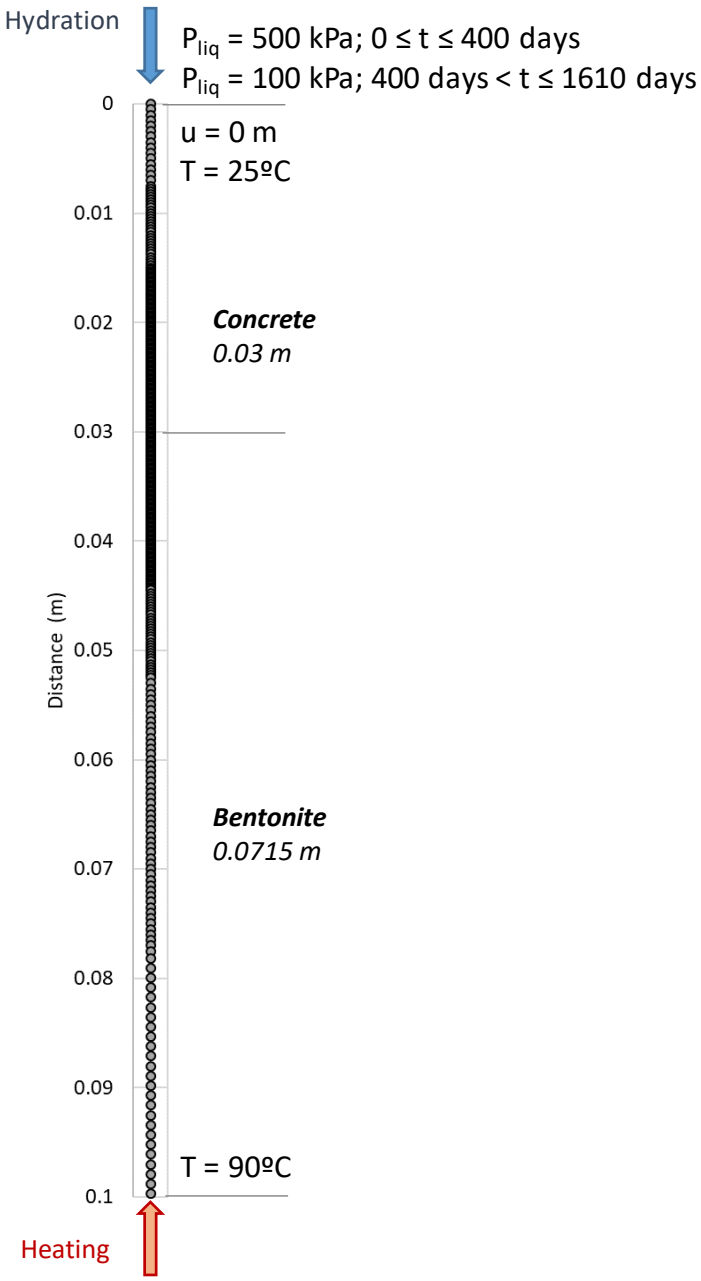

Figure 2. 1-D finite element mesh and boundary conditions for the numerical model of the HB4 column test.

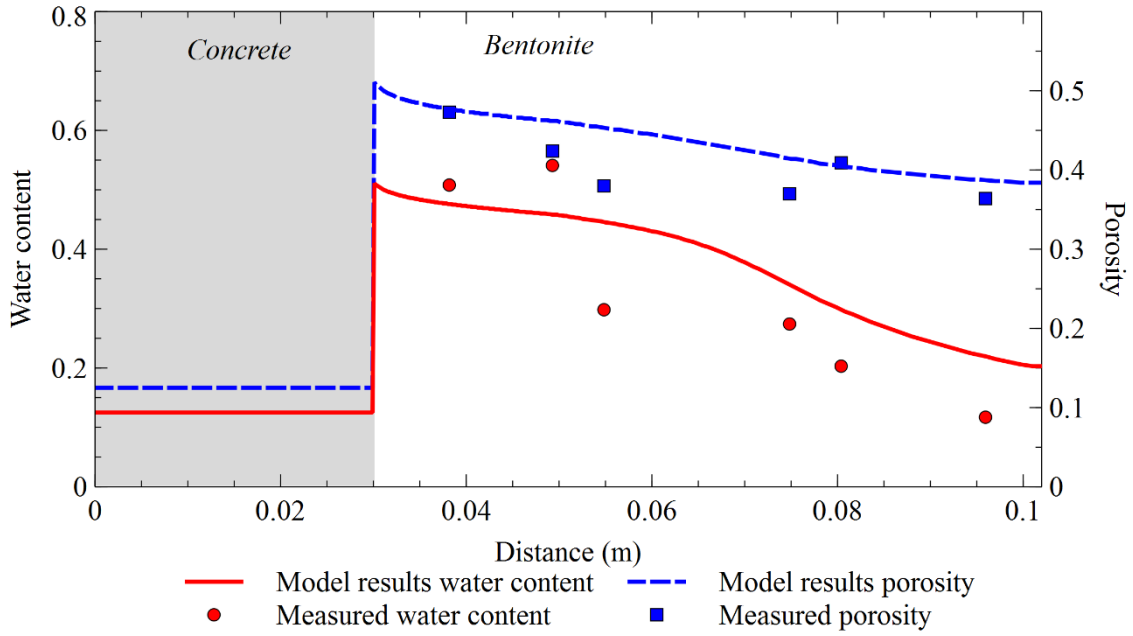

Figure 3. Computed (lines) and measured (symbols) volumetric water content and porosity in the HB4 column test at t = 1612 days (after 2 days of cooling).

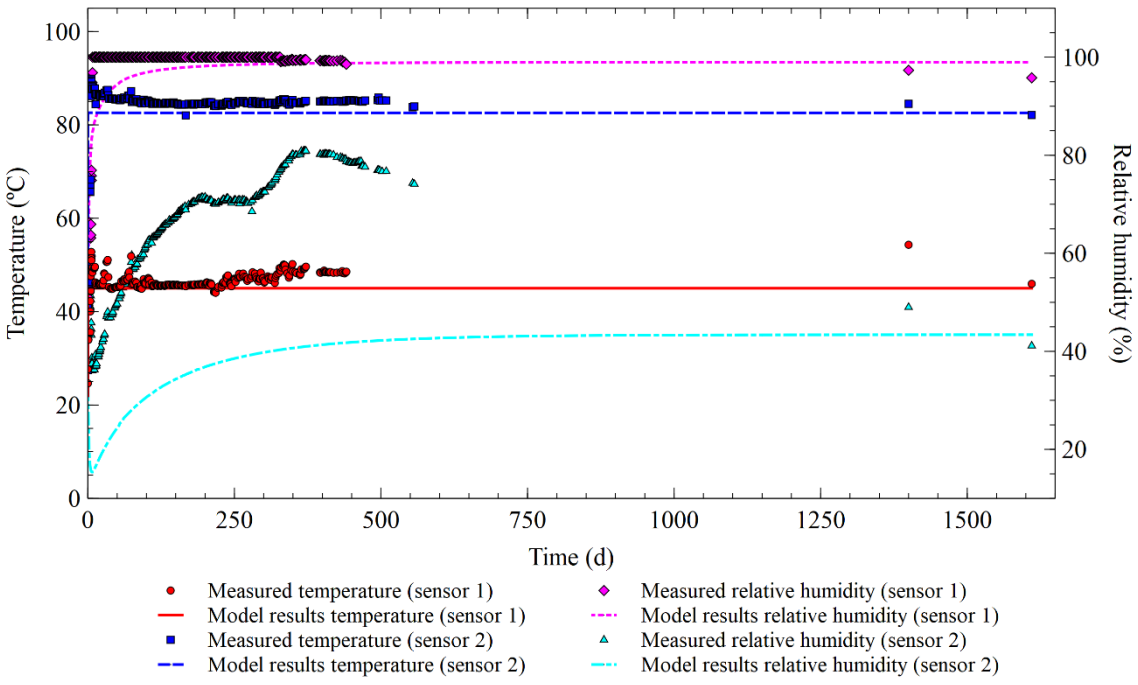

Figure 4. Time evolution of the computed (lines) and the measured (symbols) on-line temperature and relative humidity in sensor 1 (x = 5 cm) and sensor 2 (x = 9.4 cm) of the HB4 column test.

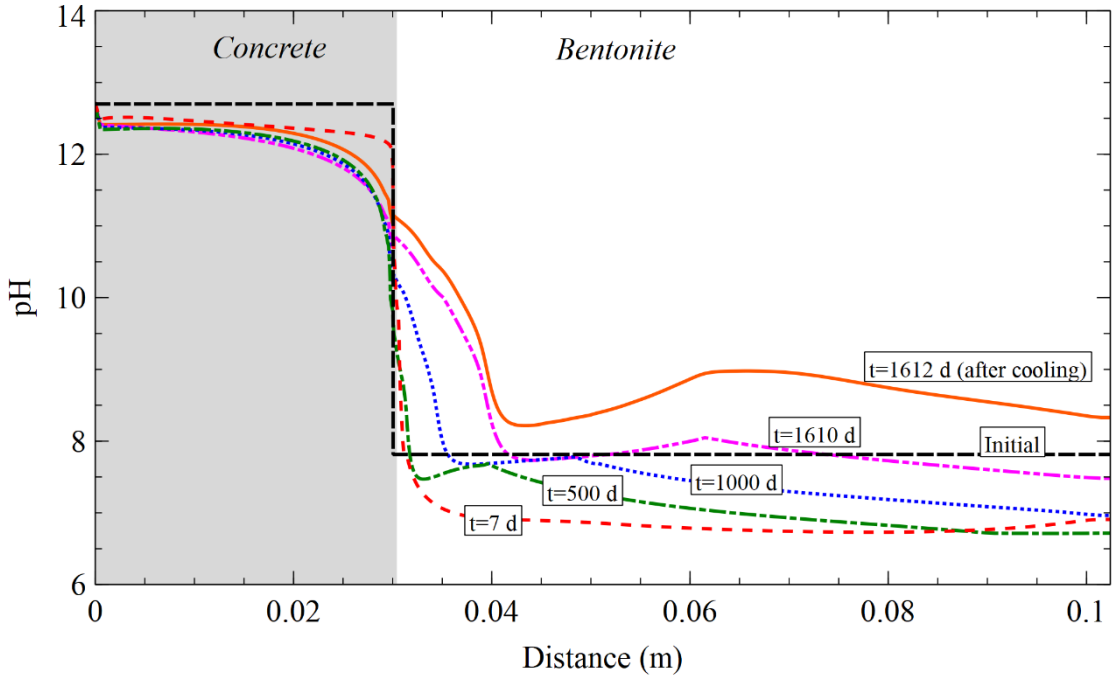

Figure 5. Spatial distribution of the computed pH in the HB4 column test at selected times.

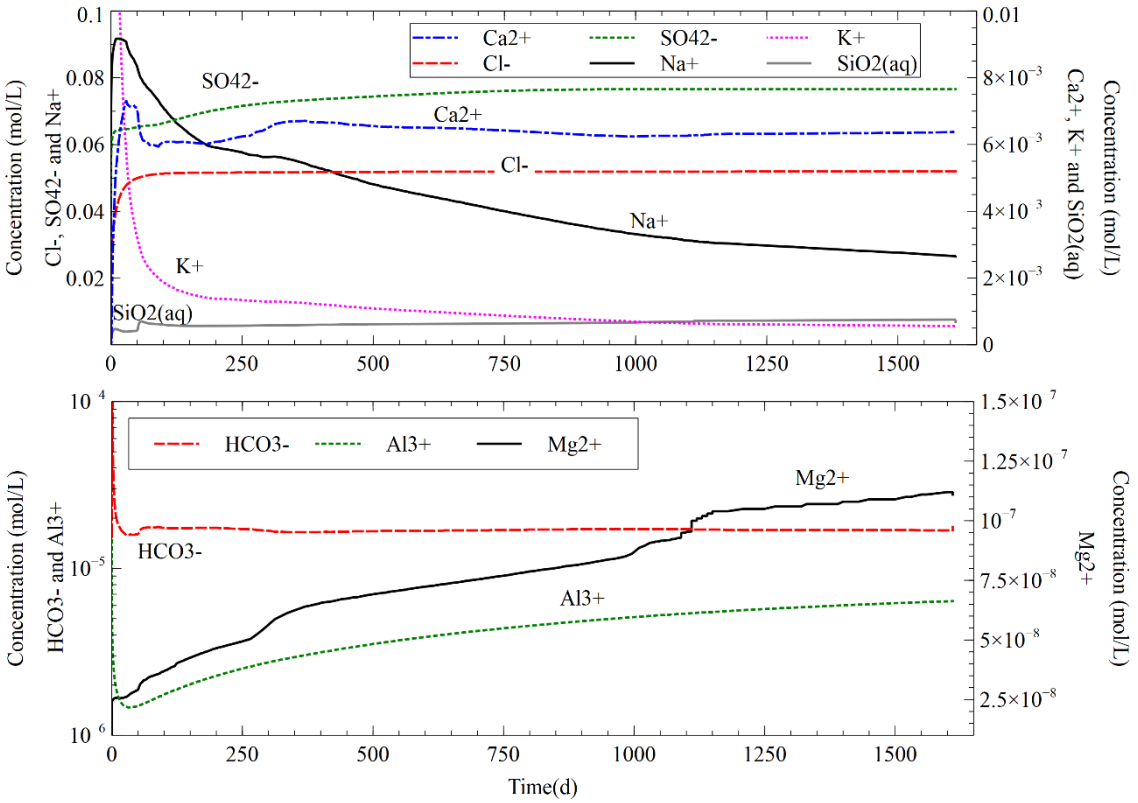

Figure 6. Time evolution of the computed concentration of dissolved Na^+, Cl^-, SO_4^{2-}, Ca^{2+}, K^+ and SiO_2(aq) (top), and HCO_3^-, Al^{3+} and Mg^{2+} (bottom) at x = 0.025 m (concrete).

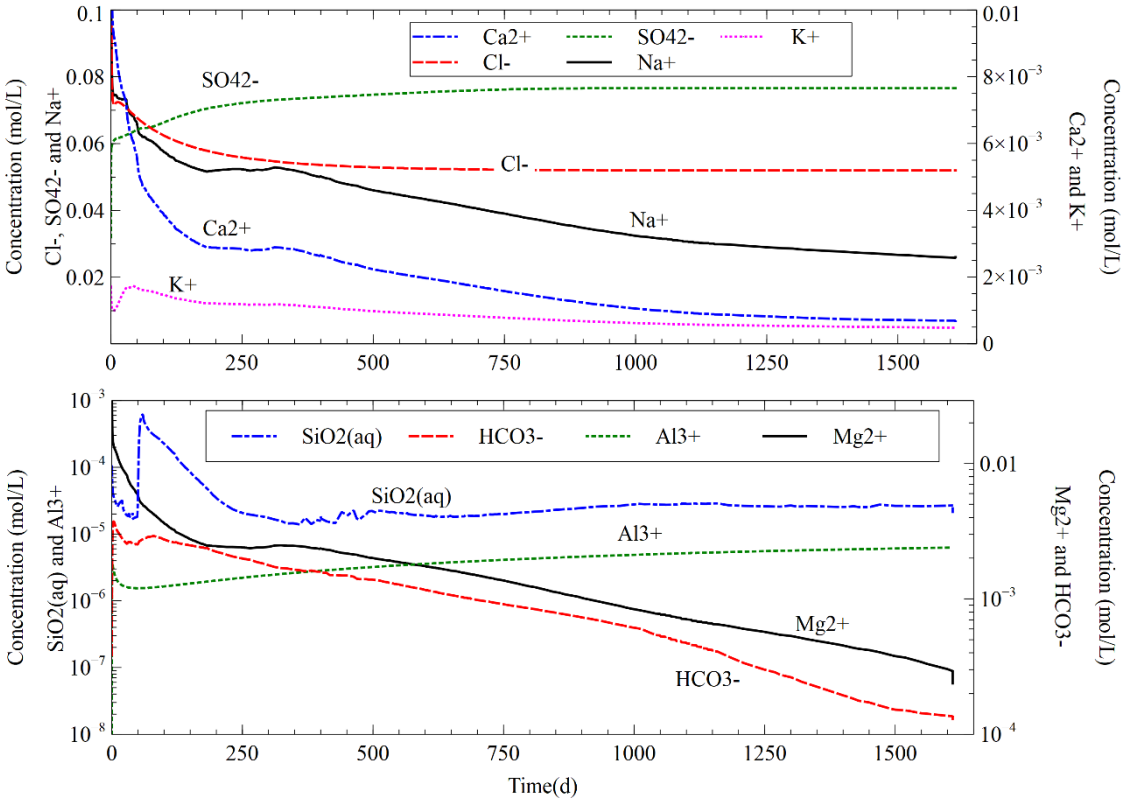

Figure 7. Time evolution of the computed concentration of dissolved Na^+, Cl^-, SO_4^{2-}, Ca^{2+} and K^+ (top), SiO_2(aq), HCO_3^-, Al^{3+} and Mg^{2+} (bottom) at x = 0.035 m (bentonite).

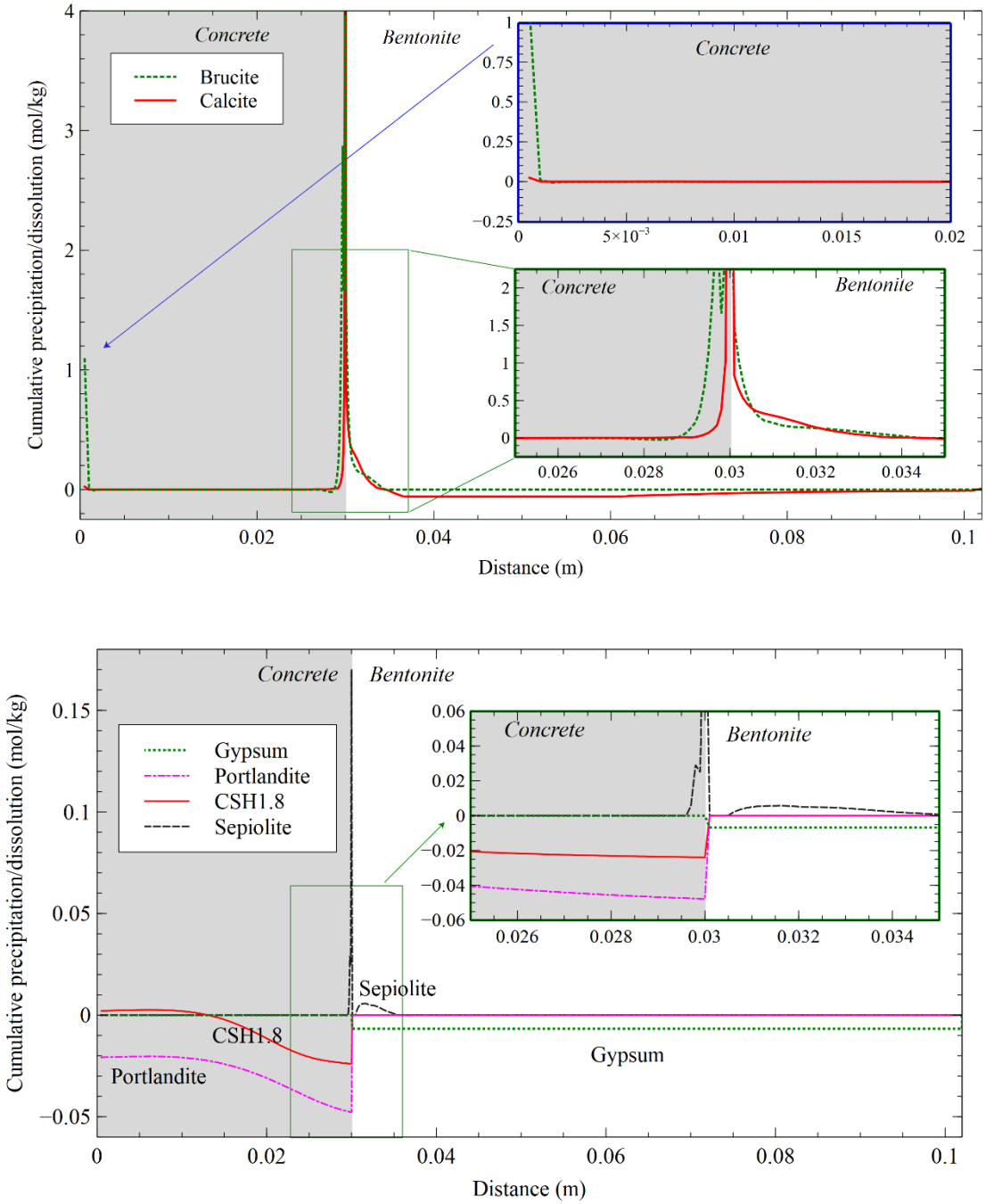

Figure 8. Cumulative dissolution/precipitation of calcite and brucite (top) and sepiolite, gypsum, portlandite and C1.8SH (bottom) in the HB4 column test at t = 1612 days (after 2 days of cooling). Positive for precipitation and negative for dissolution.

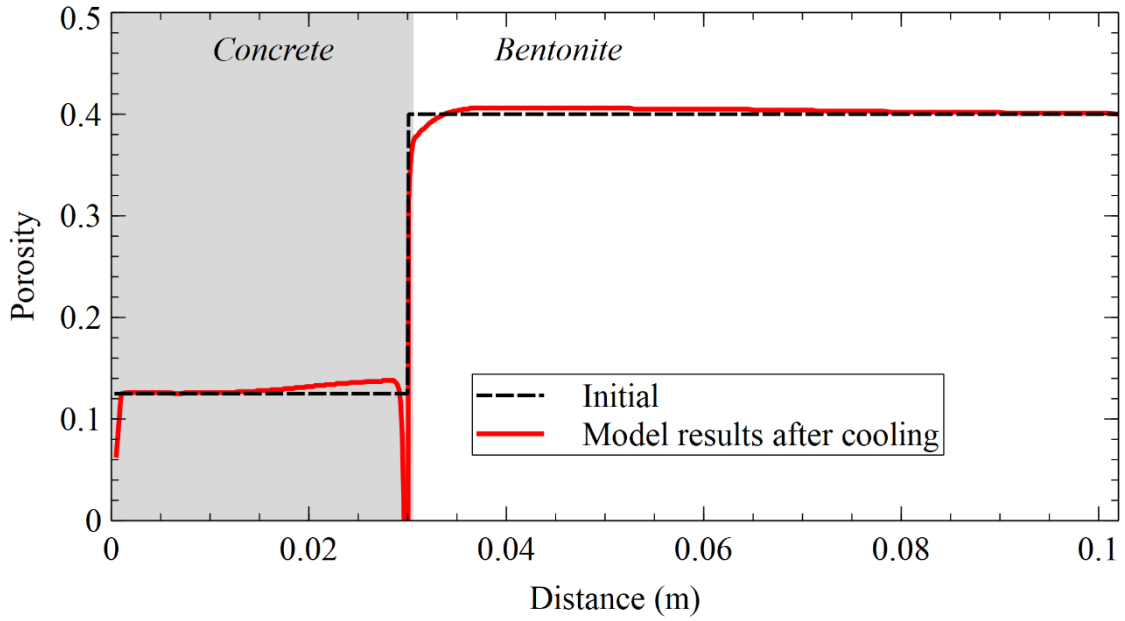

Figure 9. Initial and final porosity (after cooling) in the HB4 column test. The porosity is constant in the model. Changes in porosity are computed from mineral volume fractions.

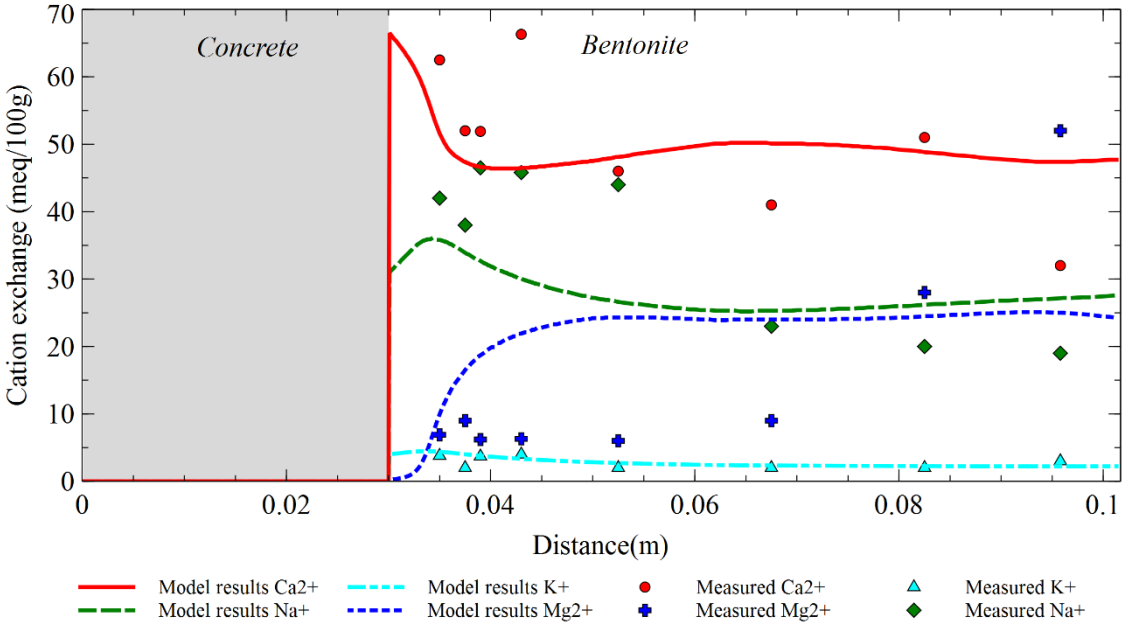

Figure 10. Spatial distribution of the computed (lines) and measured (symbols) concentrations of exchanged K^+, Ca^{2+}, Na^+ and Mg^{2+} in the HB4 column test at t = 1612 days (after 2 days of cooling).

Table 1. Experimental observations (Turrero *et al*., 2011) and THMC model results of mineral dissolution/precipitation at the end of the HB4 column test.

		Experimental observations	**Model results**
Concrete	Hydration boundary	- **Brucite** precipitates - **Calcite** precipitates	- **Brucite** precipitates (5.9% volume) - **Calcite** precipitates (0.2 % volume)
	Concrete	- **Calcite** precipitates everywhere - **C0.8SH** precipitates - **Ettringite** precipitates everywhere - **Portlandite** is nearly absent	- **Calcite** precipitates everywhere - **C0.8SH** precipitates (very small) - **Ettringite** precipitates near the hydration (less than 1% volume in 1 cm thickness) and dissolves in the rest (max of 0.4% volume in 2 cm thickness) - **Portlandite** dissolves everywhere (max of 1.6% volume at the interface)
	Concrete-bentonite interface	-**Calcite** precipitates more than in the rest of the concrete - **Ettringite** precipitates more than in the rest of the concrete	- **Calcite** precipitates more than in the rest of the concrete (53% volume) - **Ettringite** dissolves near the interface
Bentonite	Bentonite-concrete interface (d < 0.2 cm)	- **Calcite**/aragonite precipitates - **Mg-silicates** (sepiolite/saponite) - **C0.8SH** (very low) precipitation - No **ettringite** precipitation - No **anorthite** precipitation	-**Calcite** precipitates (4% volume) - **Sepiolite** precipitation (max of 0.25% volume at 0.6 cm from the interface) - **Brucite** precipitation (max of 5% volume at the interface) - **C0.8SH** precipitates (very small amount) - No **ettringite** precipitation - No **anorthite** precipitation
	Bentonite	-**Calcite** dissolves (not clear)	-**Calcite** dissolves (0.35% volume in 3 cm thickness)
	Heater interface	- **Gypsum** and **chlorite** precipitation	- **Gypsum** precipitates (less than 0.1% volume)

Table 2. Chemical reactions and equilibrium constants for aqueous complexes and minerals (Wolery, 1992), protolysis constants for surface complexation reactions (Bradbury and Baeyens, 1997) and selectivity coefficients for cation exchange reactions (ENRESA, 2006b) at 25ºC of the THCM model of the HB4 column test.

Aqueous complexes	**Log K**
$CaCO_3(aq) + H^+ \Leftrightarrow Ca^{2+} + HCO_3^-$	7.0017
$CaHCO_3^+ \Leftrightarrow Ca^{2+} + HCO_3^-$	-1.0467
$CaSO_4(aq) \Leftrightarrow Ca^{2+} + SO_4^{2-}$	-2.1111
$CaCl^+ \Leftrightarrow Ca^{2+} + Cl^-$	0.6956
$CaOH^+ + H^+ \Leftrightarrow Ca^{2+} + H_2O$	12.850
$CO_2(aq) + H_2O \Leftrightarrow H^+ + HCO_3^-$	-6.3447
$CO_3^{2-} + H^+ \Leftrightarrow HCO_3^-$	10.3288
$KSO_4^- \Leftrightarrow K^+ + SO_4^{2-}$	-0.8796
$MgCO_3(aq) \Leftrightarrow Mg^{2+} + CO_3^{2-}$	-2.9789
$MgHCO_3^+ \Leftrightarrow Ca^{2+} + HCO_3^-$	-1.0357
$MgSO_4(aq) \Leftrightarrow Mg^{2+} + SO_4^{2-}$	-2.4117
$MgCl^+ \Leftrightarrow Mg^{2+} + Cl^-$	0.1349
$NaHCO_3(aq) \Leftrightarrow Na^+ + HCO_3^-$	-0.1541
$NaSO_4^- \Leftrightarrow Na^+ + SO_4^{2-}$	-0.8200
$NaCO_3^- + H^+ \Leftrightarrow Na^+ + HCO_3^-$	9.8367
$NaCl(aq) \Leftrightarrow Na^+ + Cl^-$	0.7770
$NaOH(aq) + H^+ \Leftrightarrow Na^+ + H_2O$	14.1800
$H_3SiO_4^- + H^+ \Leftrightarrow SiO_2(aq) + 2H_2O$	9.8120
$OH^- + H^+ \Leftrightarrow H_2O$	13.9951
$CaCl_2(aq) \Leftrightarrow Ca^{2+} + 2Cl^-$	0.6436
$Ca(H_3SiO_4)_2(aq) + 2H^+ \Leftrightarrow Ca^{2+} + 2SiO_2(aq) + 4H_2O$	15.0532
$CaH_2SiO_4(aq) + 2H^+ \Leftrightarrow Ca^{2+} + SiO_2(aq) + 2H_2O$	18.5616
$CaH_3SiO_4^+ + H^+ \Leftrightarrow Ca^{2+} + SiO_2(aq) + 2H_2O$	8.7916
$MgOH^+ + H^+ \Leftrightarrow Mg^{2+} + H_2O$	11.607
$Mg_4(OH)_4^{4+} + 4H^+ \Leftrightarrow 4Mg^{2+} + 4H_2O$	39.750
$MgH_2SiO_4(aq) + 2H^+ \Leftrightarrow Mg^{2+} + SiO_2(aq) + 2H_2O$	17.4816
$MgH_3SiO_4^+ + H^+ \Leftrightarrow Mg^{2+} + SiO_2(aq) + 2H_2O$	8.5416
$NaH_3SiO_4(aq) + H^+ \Leftrightarrow 2H_2O + Na^+ + SiO_2(aq)$	8.6616
$NaHSiO_3(aq) + H^+ \Leftrightarrow H_2O + Na^+ + SiO_2(aq)$	8.3040
$KOH(aq) + H^+ \Leftrightarrow K^+ + H_2O$	14.4600
$KCl(aq) \Leftrightarrow K^+ + Cl^-$	1.4946
$KHSO_4(aq) \Leftrightarrow H^+ + K^+ + SO_4^{2-}$	-0.8136
$H_2SiO_4^{2-} + 2H^+ \Leftrightarrow 2H_2O + SiO_2(aq)$	22.9116
$H_4(H_2SiO_4)_4^{4-} + 4H^+ \Leftrightarrow 8H_2O + 4SiO_2(aq)$	35.7464
$HSiO_3^- + H^+ \Leftrightarrow H_2O + SiO_2(aq)$	9.9525
$H_6(H_2SiO_4)_4^{2-} + 2H^+ \Leftrightarrow 8H_2O + 4SiO_2(aq)$	13.4464
$HCl(aq) \Leftrightarrow H^+ + Cl^-$	0.6700
$HSO_4^- \Leftrightarrow H^+ + SO_4^{2-}$	1.9791
$Al(OH)_4^- + 4H^+ \Leftrightarrow Al^{3+} + 4H_2O$	22.1477
$Al(OH)_3(aq) + 3H^+ \Leftrightarrow Al^{3+} + 3H_2O$	16.1577
$Al(OH)_2^+ + 2H^+ \Leftrightarrow Al^{3+} + 2H_2O$	10.0991
$AlOH^{2+} + H^+ \Leftrightarrow Al^{3+} + H_2O$	5.0114
Minerals	**Log K**
$Calcite + H^+ \Leftrightarrow Ca^{2+} + HCO_3^-$	1.8487
$Anhydrite \Leftrightarrow Ca^{2+} + SO_4^{2-}$	-4.3064
$Gypsum \Leftrightarrow Ca^{2+} + SO_4^{2-} + 2H_2O$	-4.4823
$Cristobalite \Leftrightarrow SiO_2(aq)$	-3.4488
$Quartz \Leftrightarrow SiO_2(aq)$	-3.9993
$Portlandite + 2H^+ \Leftrightarrow Ca^{2+} + 2H_2O$	22.5552
$Brucite + 2H^+ \Leftrightarrow Mg^{2+} + 2H_2O$	16.2980

Sepiolite + $8H^+ \Leftrightarrow 4Mg^{2+} + 6SiO_2(aq) + 11H_2O$	30.4439
C1.8SH + $3.6H^+ \Leftrightarrow 1.8Ca^{2+} + SiO_2(aq) + 2.8H_2O$	32.4814
C0.8SH + $1.6H^+ \Leftrightarrow 0.8Ca^{2+} + SiO_2(aq) + 1.8H_2O$	10.8614
Ettringite + $12H^+ \Leftrightarrow 2Al^{3+} + 3SO_4^{2-} + 6Ca^{2+} + 38H_2O$	60.8127
Anorthite + $8H^+ \Leftrightarrow Ca^{2+} + 2Al^{3+} + 2SiO_2(aq) + 4H_2O$	24.8686
Surface complexation reactions	**Log K**
$\equiv S^SOH_2^+ \Leftrightarrow \equiv S^SOH + H^+$	-4.5
$\equiv S^SO^- + H^+ \Leftrightarrow S^SOH$	7.9
$\equiv S^{W1}OH_2^+ \Leftrightarrow \equiv S^{W1}OH + H^+$	-4.5
$\equiv S^{W1}O^- + H^+ \Leftrightarrow \equiv S^{W1}OH$	7.9
$\equiv S^{W2}OH_2^+ \Leftrightarrow \equiv S^{W2}OH + H^+$	-6.0
$\equiv S^{W2}O^- + H^+ \Leftrightarrow \equiv S^{W2}OH$	-10.5
Cation exchange	**$K_{Na\text{-}cation}$**
$Na^+ + X\text{-}K \Leftrightarrow K^+ + X\text{-}Na$	0.1456
$Na^+ + 0.5\ X_2\text{-}Ca \Leftrightarrow 0.5\ Ca^{2+} + X\text{-}Na$	0.3265
$Na^+ + 0.5\ X_2\text{-}Mg \Leftrightarrow 0.5\ Mg^{2+} + X\text{-}Na$	0.3766

Table 3. Water flow parameters for the THCM model of the HB4 column test (ENRESA, 2006a; Zheng *et al*., 2010, Villar *et al*., 2012; Villar, 2013).

	Bentonite	**Concrete**
Intrinsic permeability of the liquid, k^{il} (m^2) as a function of porosity	$k^{il} = k_0 \frac{\emptyset^3}{(1-\emptyset)^2} \frac{(1-\emptyset_0)^2}{\emptyset_0^3}$	
	with $\emptyset_o$=0.40 k_o= 2.75·10^{-21}	with $\emptyset_o$=0.125 k_o= 3.6·10^{-18}
Liquid relative permeability k^{rl} as a function of liquid saturation S_l	$k_{rl} = S_l^3$	
Retention curve: liquid saturation S_l as a function of suction Ψ (Pa)	$S_l = \frac{(1 - 9.1 \cdot 10^{-7}\Psi)^{1.1}}{[(1 + 5 \cdot 10^{-5}\Psi)^{1.22}]^{0.18}}$	$S_l = 1 + \frac{(1-0.2)}{[(1 + (3.8 \cdot 10^{-3}\Psi)^{1.23}]^{0.19}}$
Liquid viscosity (kg/m·s) as a function of temperature T (K)	$0.6612 \cdot (T - 229)^{-1.562}$	
Liquid density (kg/m^3) as a function of liquid pressure p^l and temperature	$998.2 \cdot e^{[5\cdot10^{-5}\cdot(p^l-100)-2.1\cdot10^{-4}\cdot(T-T_{ref})]}$	
Reference temperature, T_{ref} (ºC)	22	
Gas intrinsic permeability (m^2)	5·10^{-10}	
Gas relative permeability k^{rg}	$k_{rl} = (1 - S_l)^3$	
Vapor tortuosity	0.3	
Gas viscosity (kg/m·s)	1.76·10^{-5}	
Solid density (kg/m^3)	$2750 \cdot e^{[-2\cdot10^{-5}\cdot(T-T_{ref})]}$	$2360 \cdot e^{[-2\cdot10^{-5}\cdot(T-T_{ref})]}$
Thermo-osmotic permeability (m^2/K/s)	4.2·10^{-13}	

Table 4. Mechanical parameters for the THCM model of the HB4 column test (ENRESA, 2006a; Zheng *et al*., 2010).

	Bentonite	**Concrete**
Water mechanical compressibility (Pa^{-1})	5·10^{-7}	
Water thermal expansion (K^{-1})	2.1·10^{-4}	
Solid thermal expansion (K^{-1})	2·10^{-5}	
State surface parameters	$e = A + B \cdot ln\sigma' + C \cdot \ln(\Psi + P^a) + D \cdot ln\sigma' \cdot \ln(\Psi + P^a)$ A = 0.76; B = -0.052446; C = -0.0406413; D = 0.00479977	-

Table 5. Thermal parameters for the THCM model of the HB4 column test (ENRESA, 2006a; Zheng *et al*., 2010).

	Bentonite	Concrete
Specific heat of the liquid (J/kg·ºC)	4202	
Specific heat of the air (J/kg·ºC)	1000	
Specific heat of the vapor (J/kg·ºC)	1620	
Specific heat of the solid (J/kg·ºC)	835.5	789
Reference temperature (ºC)	22	
Thermal conductivity of the liquid (W/m·ºC)	1.5	
Thermal conductivity of the air (W/m·ºC)	$2.6 \cdot 10^{-2}$	
Thermal conductivity of the vapor (W/m·ºC)	$4.2 \cdot 10^{-2}$	
Thermal conductivity of the solid (W/m·ºC)	1.23	1.56
Vaporization enthalpy (J/kg)	$2.45 \cdot 10^{6}$	

Table 6. Solute transport for the THCM model of the HB4 column test (ENRESA, 2006a; Zheng *et al*., 2010).

	Bentonite	Concrete
Molecular diffusion coefficient in water $D_0(T)$ **in m²/s as a function of** T **and the molecular diffusion coefficient at the reference temperature** T_{ref} **(ºC),** $D_0(T_{ref})$	$D_o(T) = D_o(T_{ref})\frac{T}{T_0}\frac{\mu_0^l}{\mu^l}$ $D_o(T_{ref}) = 2 \cdot 10^{-10}$, (except Cl^-, $D_o(T_{ref}) = 9.2 \cdot 10^{-11}$)	
Longitudinal dispersivity (m)	0.001	0.01
Reference temperature, T_{ref} **(ºC)**	22	
Solute tortuosity τ **as a function of volumetric water content** θ **and porosity** ϕ	$\tau = \frac{\theta^{7/3}}{\emptyset^2}$	

Table 7. Chemical composition of the hydration boundary water and the initial porewaters in the bentonite and the concrete.

	Initial bentonite porewater [(1)]	Initial concrete porewater [(2)]	Synthetic Spanish Reference clay porewater [(3)]
Na^+	$1.3 \cdot 10^{-1}$	$1.6 \cdot 10^{-2}$	$1.3 \cdot 10^{-1}$
Ca^{2+}	$2.2 \cdot 10^{-2}$	$4.4 \cdot 10^{-3}$	$1.1 \cdot 10^{-2}$
Mg^{2+}	$2.3 \cdot 10^{-2}$	$1.8 \cdot 10^{-8}$	$8.2 \cdot 10^{-2}$
K^+	$1.7 \cdot 10^{-3}$	$1.0 \cdot 10^{-1}$	$8.2 \cdot 10^{-4}$
SO_4^-	$3.2 \cdot 10^{-2}$	$1.6 \cdot 10^{-2}$	$7.0 \cdot 10^{-2}$
Cl^-	$1.6 \cdot 10^{-1}$	$1.0 \cdot 10^{-5}$	$2.3 \cdot 10^{-2}$
SiO_2(aq)	$1.0 \cdot 10^{-4}$	$2.0 \cdot 10^{-5}$	$2.7 \cdot 10^{-4}$
HCO_3^-	$5.8 \cdot 10^{-4}$	$1.7 \cdot 10^{-5}$	$1.8 \cdot 10^{-3}$
Al^{3+}	$1.0 \cdot 10^{-8}$ [(4)]	$1.8 \cdot 10^{-5}$	$1.0 \cdot 10^{-8}$
pH	7.72	13.25	7.54

[(1)] Fernández et al. (2001)
[(2)] concrete porewater was calculated with EQ3 based on the concrete porewater of ENRESA (2004) and equilibrated with portlandite, calcite, brucite, ettringite and C1.8SH
[(3)] Turrero et al. (2011)
[(4)] ENRESA (2000)

Table 8. Kinetic parameters parameters for the mineral phases of the HB4 column test (Fernández *et al.*, 2009a; Palandri and Kharaka, 2004).

Mineral	**Ea (kJ/mol)**	**k_m (mol/m^2/s)**	**θ**	**η**	**n**	**σ (dm^2/L)**
Portlandite	41.86	$1.0 \cdot 10^{-8}$	1	1	-	14.732
Ettringite	41.86	$1.0 \cdot 10^{-8}$	1	1	-	$7.37 \cdot 10^{-4}$
C1.8SH	41.86	$1.0 \cdot 10^{-7}$	1	1	-	0.736
C0.8SH	41.86	$1.0 \cdot 10^{-7}$	1	1	-	0.736
Quartz	95.79	$5.13 \cdot 10^{-17}$	1	1	0.55	7.36
Cristobalite	65.0	$5.0 \cdot 10^{-13}$	1	1	-	0.147